The size distribution of Jupiter's main ring from Galileo imaging and spectroscopy

Shawn M. Brooks,[a,*] Larry W. Esposito,[a] Mark R. Showalter,[b] and Henry B. Throop [c]

[a] *Department of Astrophysical and Planetary Sciences, University of Colorado, Boulder, CO 80309, USA*
[b] *Center for Radar Astronomy, Stanford University, Stanford, CA 94305, USA*
[c] *Department of Space Studies, Southwest Research Institute, Boulder, CO 80302, USA*

Abstract

Galileo's Solid State Imaging experiment (SSI) obtained 36 visible wavelength images of Jupiter's ring system during the nominal mission (Ockert-Bell et al., 1999, Icarus 138, 188–213) and another 21 during the extended mission. The Near Infrared Mapping Spectrometer (NIMS) recorded an observation of Jupiter's main ring during orbit C3 at wavelengths from 0.7 to 5.2 µm; a second observation was attempted during orbit E4. We analyze the high phase angle NIMS and SSI observations to constrain the size distribution of the main ring's micron-sized dust population. This portion of the population is best constrained at high phase angles, as the light scattering behavior of small dust grains dominates at these geometries and contributions from larger ring particles are negligible. High phase angle images of the main ring obtained by the Voyager spacecraft covered phase angles between 173.8° and 176.9° (Showalter et al., 1987, Icarus 69, 458–498). Galileo images extend this range up to 178.6°. We model the Galileo phase curve and the ring spectra from the C3 NIMS ring observation as the combination of two power law distributions. Our analysis of the main ring phase curve and the NIMS spectra suggests the size distribution of the smallest ring particles is a power law with an index of 2.0 ± 0.3 below a size of ~ 15 µm that transitions to a power law with an index of 5.0 ± 1.5 at larger sizes. This combined power law distribution, or "broken power law" distribution, yields a better fit to the NIMS data than do the power law distributions that have previously been fit to the Voyager imaging data (Showalter et al., 1987, Icarus 69, 458–498). The broken power law distribution reconciles the results of Showalter et al. (1987, Icarus 69, 458–498) and McMuldroch et al. (2000, Icarus 146, 1–11), who also analyzed the NIMS data, and can be considered as an obvious extension of a simple power law. This more complex size distribution could indicate that ring particle production rates and/or lifetimes vary with size and may relate to the physical processes that control their evolution. The significant near arm/far arm asymmetry reported elsewhere (see Showalter et al., 1987, Icarus 69, 458–498; Ockert-Bell et al., 1999, Icarus 138, 188–213) persists in the data even after the main ring is isolated in the SSI images. However, the sense of the asymmetry seen in Galileo images differs from that seen in Voyager images. We interpret this asymmetry as a broad-scale, azimuthal brightness variation. No consistent association with the magnetic field of Jupiter has been observed. It is possible that these longitudinal variations may be similar to the random brightness fluctuations observed in Saturn's F ring by Voyager (Smith et al., 1982, Science 215, 504–537) and during the 1995 ring plane crossings (Nicholson et al., 1996, Science 272, 509–515; Bosh and Rivkin, 1996, Science 272, 518–521; Poulet et al., 2000, Icarus 144, 135–148). Stochastic events may thus play a significant role in the evolution of the jovian main ring.

1. Introduction

Among the many successes of the Galileo mission to Jupiter was the acquisition of a high-quality, diverse set of observations of the rings of Jupiter. Jupiter's rings are optically thin and contain large numbers of dust-sized particles that are most easily seen when backlit by the Sun. Therefore, they are readily detectable by spacecraft, which can image them from such a geometry. The rings were targeted in 25 observations made by Galileo with its Solid State Imaging (SSI) experiment during the nominal mission; they fortuitously appeared in another eleven SSI images (Ockert-Bell et al., 1999). Another 21 observations of the ring were

---

* Corresponding author. Now at Jet Propulsion Laboratory, California Institute of Technology, 4800 Oak Grove Drive, M/S 230-205, Pasadena, CA 91109, USA. Fax: (818)-393-4495.

E-mail address: shawn.m.brooks@jpl.nasa.gov (S.M. Brooks).

taken during the Galileo Extended Mission. Galileo's Near Infrared Mapping Spectrometer (NIMS) also successfully imaged the rings during orbit C3. Analysis of these detailed observations of the rings have improved our understanding of this unique ring system.

The first evidence that Jupiter possesses a ring system came from the Pioneer 10 and 11 particle flux measurements (Fillius et al., 1975; Acuña and Ness, 1976). However, the existence of a ring system around Jupiter was not proven until Voyager 1's Imaging Science Subsystem (ISS) returned a smeared, multiply exposed image of the main ring in March 1979. The 25 ring images produced by Voyagers 1 and 2 through its clear, orange, green and violet filters at a variety of viewing angles, revealed the ring system's main characteristics (Showalter et al., 1987). A relatively bright main ring with a normal optical depth, $\tau \sim 10^{-6}$, circumscribes a vertically-extended halo. Although the halo has a normal optical depth comparable to that of the main ring, its vertical extent means that it appears much fainter than the main ring in spacecraft images taken near Jupiter's equatorial plane. A faint, broad ring, now known as the "gossamer" ring, was discovered with Voyager ISS data (Showalter et al., 1985). Galileo SSI images revealed the gossamer ring to actually be two distinct rings (Ockert-Bell et al., 1999). Burns et al. (1999) showed that the gossamer rings are dynamically linked to Jupiter's moons Amalthea and Thebe.

The rings have been observed from the ground in visible and near-infrared wavelengths. Infrared observations of Amalthea and the main ring between 0.9 and 2.5 µm were obtained by Neugebauer et al. (1981) with the Infrared Telescope Facility at Mauna Kea Observatory. Nicholson and Matthews (1991) reported on 119 images of the main ring, Metis and Adrastea taken at 2.2 µm with the Caltech Cassegrain infrared camera and the Hale telescope in 1988. From observations taken with the W.M. Keck telescope during the Jupiter ring plane crossing of 14 August 1997 de Pater et al. (1999) identified all three components of the ring system. Meier et al. (1999) describe near-infrared observations of the ring with the near infrared camera and multi-object spectrometer (NICMOS) on the Hubble Space Telescope. Cassini's Imaging Science Subsystem (ISS) took hundreds of images of the ring as it flew through the jovian system during December 2000 and January 2001 on its way to Saturn. The Cassini ISS ring images were taken at nine different wavelengths, from the ultraviolet to the near-infrared, and at three polarizations. These observations cover a variety of phase angles from 0.5° up to 120°. The best spatial resolution obtained by ISS was ∼ 58 km/pixel (Throop and Porco, 2001; Porco et al., 2002).

Based on their analysis of Voyager imaging data, Showalter et al. (1987) produced a phase curve for Jupiter's main ring. Their photometric models of its phase curve suggested that the ring particles' size distribution follows a power law with an index of 2.5 ± 0.5. Showalter et al. (1987) also found that ratios of the main ring's brightness at orange and violet wavelengths indicate the power law index to be 2.2 ± 0.2.

Because NIMS is sensitive to longer wavelengths, observations made with NIMS probe larger particles in the size distribution (see Section 4.1). From their analysis of the C3 NIMS observation, McMuldroch et al. (2000) argued that the size distribution is actually a log-normal distribution centered at 4.5 microns superposed on a steep power-law with an index of 3.9 ± 0.2.

Here we report on our analysis of Galileo visible and infrared data and place our work in the context of earlier results. Considering both the SSI and NIMS data allows us to take advantage of the range in phase angles of the SSI observations and the range in wavelengths of the NIMS observations to constrain the size distribution of the dust-sized particles in the main ring. We reconcile the results of previous analyses of the Voyager ISS data and the Galileo NIMS data which seem to contradict one another. Furthermore, our derived size distribution may yield insight into the dynamics and evolution of the particles comprising Jupiter's main ring.

2. SSI observations

2.1. SSI images

Galileo's Solid State Imaging experiment consists of a 1500-mm focal length telescope with an 800×800 pixel CCD at its focus (Belton et al., 1992). Each pixel subtends 0.01 mrad, giving the SSI a total 8 mrad field of view. The SSI is also equipped with 8 filters, having effective wavelengths ranging from 414 nm up to 990 nm (Klaasen et al., 1984, 1997, 1999). However, all targeted observations of the faint ring system were made through the clear filter to keep exposure times short.

Various components of the ring system were imaged during orbits C3, G8, C10, E11, E17, G28, G29, and I32. We have restricted our photometric analysis to eight of the 13 images obtained during orbit C3. Taken over a span of three hours on 9 November 1996, while the spacecraft was in Jupiter's shadow, these represent the highest signal-to-noise images of Jupiter's main ring. In these images, the phase angle, the angle subtended by a line from the observer to the object and a line from the object to the illumination source (the Sun in this case), varies between 175° and 179°. Images from the nominal mission (orbits up through E11) were taken at phase angles of 83° and higher; phase angles in extended mission images (orbits after E11) span a range of 5° up to 82°. While the C3 images were taken Galileo was ∼ 0.46° above the ring plane and ranged between 2.25×10^6 km ($31.5R_J$) and 2.33×10^6 km ($32.6R_J$) from Jupiter (Ockert-Bell et al., 1999). The resolutions in these images are some of the best ever obtained of the main ring. The subset of the ring images we analyzed contained three with a resolution of 23 km/pixel, two at 24 km/pixel, and three with 46 km/pixel resolution (Ockert-Bell et al., 1999). This information is summarized in Table 1.

Picture ID	Exposure (msec)	Resolution km/pixel	Range (10^6 km)	Emission angle (degrees)	Phase angle (degrees)	Observation time
s0368974113	95.8	23	2.25	89.53	178.1–178.6	1996 Nov 09 04:15:12
s0368974126	195.8	23	2.25	89.54	177.8–178.2	1996 Nov 09 04:15:21
s0368974139	195.8	23	2.25	89.55	177.4–177.9	1996 Nov 09 04:15:29
s0368975900	395.8	46	2.27	89.54	175.7–176.2	1996 Nov 09 04:33:16
s0368975922	395.8	46	2.27	89.54	176.1–176.6	1996 Nov 09 04:33:30
s0368975945	262.5	46	2.27	89.54	176.5–177.0	1996 Nov 09 04:33:46
s0368991900	95.8	24	2.33	89.54	176.1–176.6	1996 Nov 09 07:15:02
s0368992339	195.8	24	2.33	89.54	177.1–177.6	1996 Nov 09 07:19:31

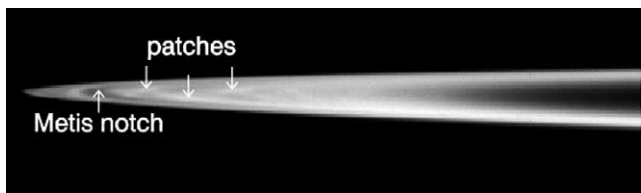See also Ockert-Bell et al. (1999).

Fig. 1. Galileo SSI Image s0368974139, centered on the western ansa of the main ring, reveals fine structure in the main ring of Jupiter, including the Metis notch and bright patches not seen in Voyager images. It has been slightly stretched to emphasize the bright patches and the Metis notch. Phase angles in this image range from 177.4°–177.9°. Similar features are visible in image s038991900, an image of the ring's eastern ansae (see Ockert-Bell et al., 1999, Fig. 3).

Image s0368974139, shown in Fig. 1, shows some of the details revealed in SSI images of the main ring. The main ring possesses a sharp outer boundary and a more diffuse inner one, consistent with its appearance in Voyager images. The Metis notch, discussed in Ockert-Bell et al. (1999), clearly stands out. A similar feature is visible in high-phase angle Voyager images (Showalter et al., 1987). Its location relative to Metis suggests a relationship with that satellite, although the nature of that relationship is not clear. Bright patches in the main ring that were not seen in Voyager data also stand out in Galileo images. Their origin is not understood. These features are also discussed in Ockert-Bell et al. (1999).

2.2. Image calibration and reduction

The ring images and calibration files were obtained from the Planetary Data System. Flat field and dark current frames were subtracted from the raw data, which were also corrected for known camera blemishes and then radiometrically converted to normalized reflectance, or I/F, where I is the intensity measured by the camera and πF is the solar flux incident on the rings. The stated uncertainty in the absolute calibration of the camera through the clear filter is 5.2% and the effective wavelength for scenes under solar illumination is 624.9 nm (Klaasen et al., 1999).

Due to Galileo's low elevation above the ring plane and the low optical depths of all the ring system components, pixels in the main ring in the original images also contain contributions from the halo and gossamer rings. In order to accurately measure the brightness of the main ring, it was necessary to remove this signal and that of any scattered light in the images. To accomplish this, we subtracted the background in a manner similar to that described in Meier et al. (1999).

Figure 2 illustrates this process. Because each column of pixels in the analyzed images is roughly perpendicular to the ring plane, we were able to estimate the background by masking out the main ring and interpolating through the remaining pixels column by column. To create the mask, the main ring was modeled as a simple cylindrical ring, rectangular in cross-section, with an inner radius of 122,000 km and an outer radius of 129,500 km. The thickness of the ring for this mask was taken to be 350 km, slightly thicker than the upper limit determined by Showalter et al. (1987) from Voyager high-phase angle images. The "mask ring" was chosen to be larger than the actual ring to avoid subtracting light from the main ring in the images, but still be small enough to satisfactorily model the background. In each image sample, any pixel containing a line of sight through this hypothetical ring was masked out. Column by column, vertical scans through the image were taken and pixels not masked out were fit with a sixth-degree polynomial. The interpolations through the masked-out pixels were then used to produce an "image" of the background by combining the fits to each vertical scan. A boxcar average was applied to the background image which was then subtracted from the original image. This process was repeated for each of the SSI images used in our analysis. The top panel of Fig. 2a is one of the C3 images before any manipulation. The middle panel of this figure shows an example of our estimated background. The results of this process are shown in the final panel of Fig. 2a. Residuals in pixels outside our mask region suggest that this process successfully removed signals from the background and the halo. Before the subtraction I/F values outside the mask region were $\sim (5.0 \pm 1.0) \times 10^{-3}$. Afterwards, residuals beyond the mask region were typically $\lesssim 1 \times 10^{-4}$.

2.3. Photometry

Having isolated the main ring in this fashion, we took radial cuts with longitudinal widths of 4° through the

(a)

(b)   (c)
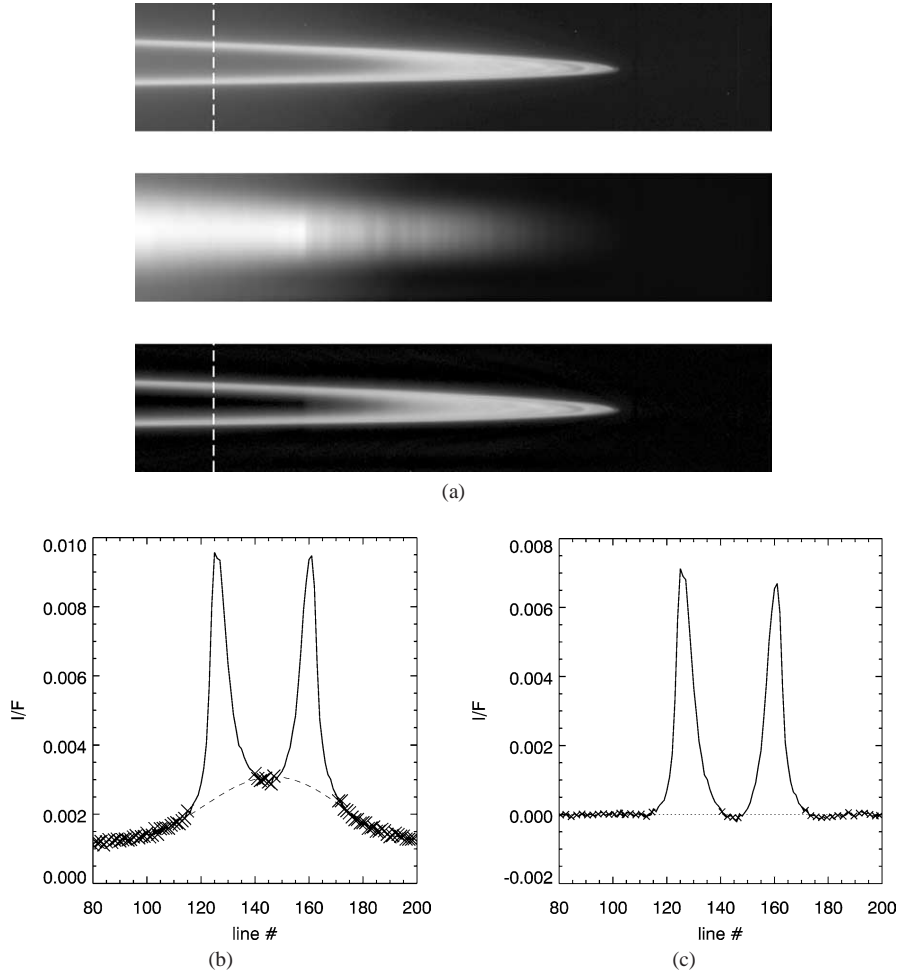
Fig. 2. A profile along the dashed line in the top image of (a) is plotted in (b). The middle panel of (a) is an image showing our model of the halo and background light. The bottom panel shows the result of subtracting the middle panel from the top one. The combined signal from the main ring and halo is plotted in (b). Points outside the mask region used to model the halo are marked with "×" symbols. Our estimate of the background and halo contribution made by interpolating through these points is marked with a dashed line. (c) Is a plot along the dashed line in the bottom image of (a) after the main ring has been isolated and is a graphical representation of the results of this process.

processed images (e.g., the bottom panel of Fig. 2a) to produce radial profiles of the main ring, as shown in Fig. 3.

Interior to a radius of 119,000 km, no discernible signal from the ring halo remains after the main ring has been isolated. Even without the background removal process, the bright patches visible within the main ring show up as small peaks along the ring profile. There is a significant decrease in the ring's brightness in the vicinity of Metis' orbit, which is bounded on its outer edge by a bright annulus of ring material. This is the Metis notch depicted in Fig. 1. It is seen in all Galileo images of the rings' ansae. Radial scans of the ring from high-phase angle Voyager images show a similar feature (see Showalter et al., 1987, Fig. 3.2), but the dip in brightness is not as pronounced and the increase in brightness interior to the main ring is larger, relative to the peak exterior to the Metis notch, than in Galileo images.

To consistently calculate an average normalized reflectance for the ring, we computed the ring's equivalent width by summing the area under each of these radial profiles. This quantity was then divided by the ring's width,

which was taken to be 6500 km (Ockert-Bell et al., 1999). For low optical depths, such that $\tau/\mu \ll 1$ (where $\mu \equiv |\cos\epsilon|$ and ϵ, the emission angle, is the angle between the ring plane normal and the direction to the observer), the reflectance is related to ϖ_0, the ring particle single-scattering albedo and $P(\theta)$, the phase function of the ring particles, and τ via

$$\frac{I}{F} = \frac{\tau \varpi_0 P(\theta)}{4\mu} \qquad (1)$$

(Chandrasekhar, 1960; Cuzzi et al., 1984). The phase function varies with scattering angle, θ, defined as the supplement of the phase angle. μ accounts for the oblique viewing geometry which is slightly different in each image. So long as the equivalent width is calculated consistently, Eq. (1) can be used to relate observations at any emission angle (excepting, of course, the case where $\mu = 0$). Computed in this fashion, the normalized reflectance, $\tau \varpi_0 P$, is thus ideal for comparing images taken at different viewing angles. Figure 4 shows the ring's normalized reflectance de-
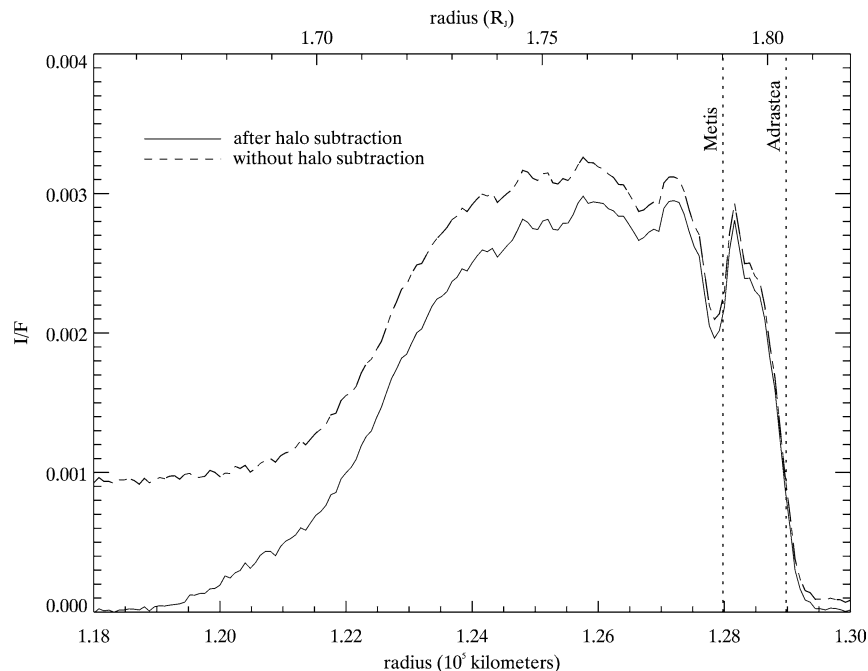
Fig. 3. The normalized reflectance of the main ring as derived from image s0368991900 is plotted as a function of distance from Jupiter. The dashed line is the ring's profile before scattered light has been removed; the solid line represents the profile after the image has been processed to removed the scattered light. In contrast with the sharply defined outer edge, the main ring's inner boundary is gradual. For reference, the locations of the semimajor axes of the orbits of Metis and Amalthea have been plotted as well. A similar plot appears in Ockert-Bell et al. (1999).

rived from Galileo SSI data plotted alongside Voyager ISS data (Showalter et al., 1987).

The coverage of the ring's phase curve in the visible has been extended from the Voyager range of 174.0° to 176.8° (Showalter et al., 1987) up to a phase angle of $\sim 178.3°$ (a scattering angle of 1.7°). The phase coverage of the Galileo SSI images and the Voyager ISS images nearly overlap at a scattering angle of 4.2°. The reflectances derived from the Voyager orange filter and the Galileo clear filter data are roughly equal where the phase ranges of the two data sets overlap. This is consistent with these two filters having similar effective wavelengths (but, it should also be noted that the two filters have bandpasses with very different widths). The Galileo clear filter data are roughly twice as bright as the Voyager clear filter data at similar phase angles. Although the Voyager and Galileo clear filter data are offset from one another, they suggest a phase behavior with a consistent slope throughout the range in scattering angle.

Since Showalter et al. (1987) used the Voyager clear filter data set in the same manner we did with the Galileo data, it is of interest to investigate why this offset exists. A small portion of this offset (7%) is due to the fact that we have taken the ring to be 6500 km wide, whereas Showalter et al. (1987) used a distance of 7000 km. In addition, the bandpasses of the Galileo and Voyager clear filters are different. The central wavelength of the clear filters used by the Voyager cameras is 0.46 μm and the passband of the wide angle camera clear filter is double-peaked (Danielson et al., 1981). The effective wavelength of the SSI clear filter, on the other hand, is 0.6249 μm (Klaasen et al., 1999). For a power-law

distribution of particles with an index q (see Eq. (8)), we have from Showalter (1985),

$$\frac{\tau_1}{\tau_2} = \left(\frac{\lambda_1}{\lambda_2}\right)^{3-q}.$$ (2)

From this, one would expect, for $q < 3$, these particles to appear brighter (i.e., have a higher optical depth) at longer wavelengths. However, for an index of 2.0, the predicted increase is only $\sim 36\%$ for the effective wavelengths given above. Some portion of the offset may be attributable to inconsistencies in the relative calibration of the two cameras. The Voyager orange data are offset from the violet filter data by almost a factor of two, a difference comparable to that between the Voyager and Galileo data. It is also possible that some portion of this discrepancy is due to some change in the ring's brightness between the Voyager encounters and the Galileo mission.

3. NIMS observations

3.1. NIMS data

Galileo's Near Infrared Mapping Spectrometer is equipped with an 800-mm focal length, Ritchey–Chrétien telescope and an array of 17 individual detectors, each of which covers a portion of the instrument's 0.7–5.2 μm wavelength range, located at the telescope's focal plane. The telescope's secondary mirror scans through 20 positions, producing 20 contiguous pixels, each with a 0.5 × 0.5 mrad field of view,
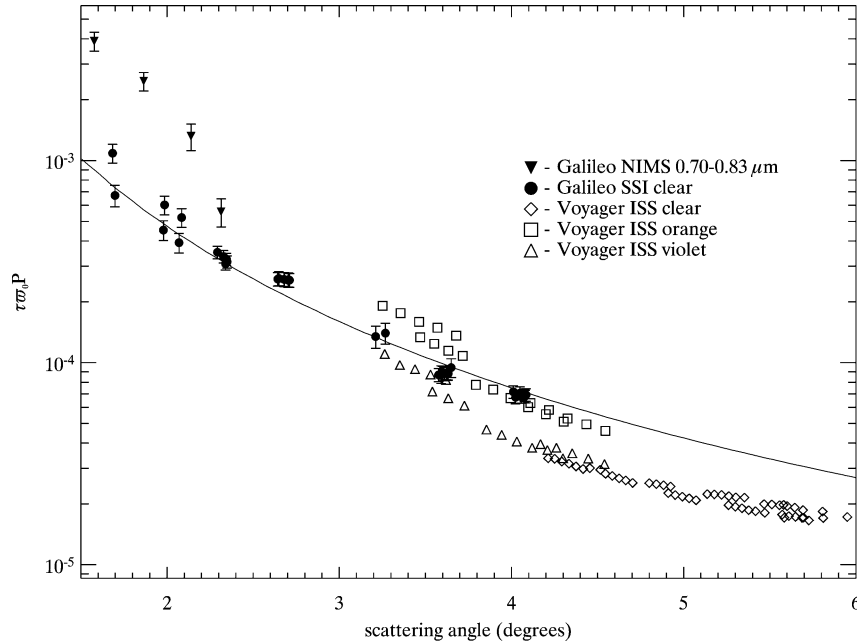
Fig. 4. The phase curve of the main ring derived from Galileo SSI data is consistent with the phase curve derived from Voyager ISS images. The Galileo data were all derived with images taken through the clear filter, which is a broadband filter with an effective wavelength of 0.6249 μm under solar illuminated scenes (Klaasen et al., 1999). The Voyager clear filter has an effective wavelength of 0.5 μm. The orange and violet filters of the Voyager ISS camera pass light primarily at 0.61 and 0.43 μm, respectively (Showalter et al., 1987). The solid line represents our fit to the Galileo SSI observations for an ensemble of particles with a power law size distribution with $q = 2$. Also plotted for comparison is the average ring brightness seen by NIMS between 0.70 and 0.83 μm at four phase angles.

along one scan direction. This direction defines the instrument's cross-cone direction. Slewing the spacecraft's scan platform provides the second spatial, or cone, dimension. As the mirror scans, a slewing plane grating disperses radiation onto each of the 17 detectors, producing two spatial dimensions of information and one spectral (Carlson et al., 1992).

Two NIMS observations of the rings were attempted during the Galileo mission. A low signal-to-noise, multispectral image of the main ring was produced during orbit C3 as the spacecraft passed behind Jupiter. Recorded between two SSI imaging sequences that also targeted the main ring, this NIMS observation took ~ 9 minutes to record. The C3 data cube was taken with a spectral resolution of 0.0125 μm below ~ 1 and 0.025 μm above ~ 1 μm (Carlson et al., 1992). The observation, which contains 20×122 overlapping pixels, was meant to cover 102 wavelengths, but by this point in the mission, one of the detectors had failed and no useable data were returned at 6 wavelengths between 2.36 and 2.67 μm. At the time the C3 observation was made Galileo was just $0.46°$ above the ring plane and $\sim 2.26 \times 10^6$ km ($31.6 R_J$) from the center of Jupiter. During the observation the spacecraft was at a phase angle of $\sim 178°$. The resolution is 1130 km/pixel at this distance from Jupiter. Because of the spacecraft's low elevation angle and the observation's relatively low spatial resolution, the arms of the ring were not individually resolved during the C3 observation.

Four slices through this data cube are shown in Fig. 5. Three "images" of the ring, built up pixel-by-pixel, appear

in Fig. 5a. Farthest from Jupiter, the highly foreshortened ring is a distinctly bright stripe appearing in line 10 of the images. Closer to the planet, the ring becomes visible in adjacent pixels as well, due to the increasing projected distance between its near and far arms. Figure 5b shows a projection in wavelength space, along line 10.

The second NIMS observation was attempted during orbit E4 on 20 December 1996. The observation took roughly one minute to record and resulted in a data cube containing 20×14 pixels at 96 wavelengths. During this observation the spacecraft was $\sim 0.5°$ above the ring plane and $\sim 1.58 \times 10^6$ km ($22.1 R_J$) from Jupiter. At a phase angle of approximately $152°$, the ring was below the detection limit of NIMS. Nowhere in this data cube is the ring unambiguously identifiable. However, analysis of this observation still provides an upper limit on the main ring's optical depth. Phase angle, emission angle, range, and resolution information for the two NIMS observations is summarized in Table 2.

3.2. Data reduction

3.2.1. C3 NIMS data

The calibrated C3 and E4 NIMS cubes were obtained through the Rings Node of Planetary Data System. Brightnesses in these calibrated data are expressed as normalized reflectance as well. From the C3 data cube, we produced four spectra by summing pixels along the cross-cone direction, which is orthogonal to the ring plane, at four
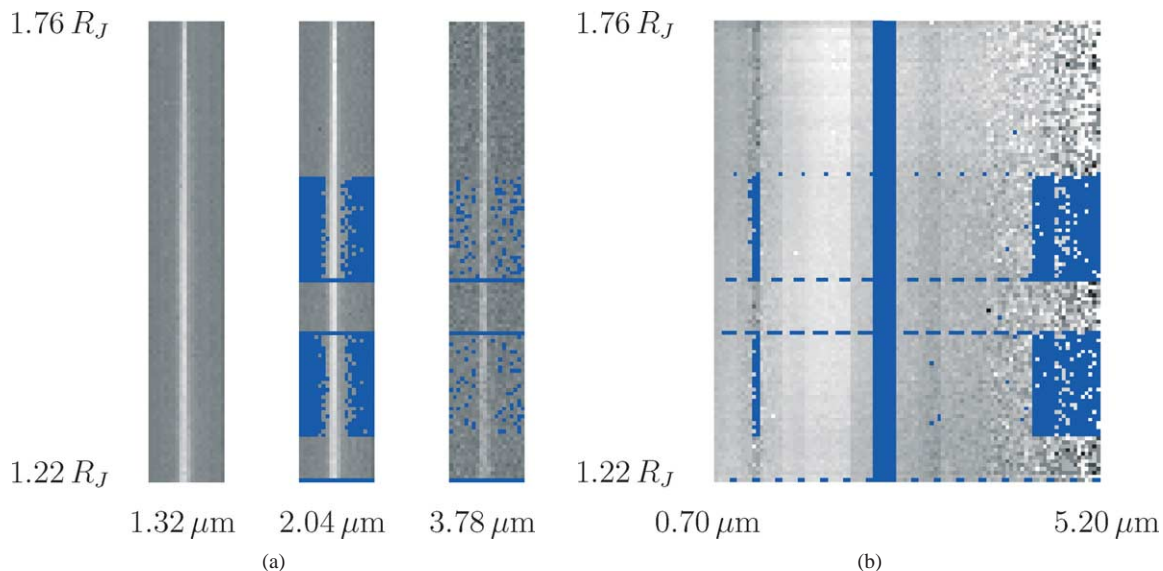
Fig. 5. Four slices through the NIMS data cube from the C3 ring observation. (a) shows the ring at three wavelengths: 1.32, 2.04, and 3.78 μm. The ring arms were not individually resolved and, as a result, the main ring appears as a bright stripe in the center of each image. (b) is a projection along the ring plane, corresponding to the bright stripe in the images of (a). The distances represent the minimum distance to Jupiter along lines of sight through the ring plane. Blue represents data that were not returned in order to save on downlink (McMuldroch et al., 2000).

Table 2
NIMS observation details

Observation ID	Resolution (pixels/degree)	Range (10^6 km)	Emission angle (degrees)	Phase angle[a] (degrees)	Observation start/end time
C3RNMRING_01A	2.207	2.26	89.54	177.69 (A) 177.86 (B) 178.14 (C) 178.42 (D)	1996 Nov 09 04:19:05 04:28:01
E4RNMRING_01B	3.150	1.58	89.54	152	1996 Dec 20 17:16:23 17:17:20

[a] The phase angles listed for observation C3RNMRING_01A pertain to the phase angles of the four spectra analyzed.

separate locations in the ring at each wavelength. Carlson et al. (1997) employ such a summation in their analysis of an under-resolved NIMS observation of one of the Comet Shoemaker–Levy 9 impacts. The spectra we analyzed correspond to distances of 1.72, 1.61, 1.43, and $1.24 R_J$, from the center of the planet, respectively. More precisely, these distances represent the minimum distance to the planet's center along the line of sight of the pixel. These locations roughly correspond to locations A, B, C, and D of McMuldroch et al. (2000).

Because of the low resolution and low elevation angle of this observation, each NIMS pixel has a very large footprint in the ring plane. This large footprint and the low spatial resolution of this observation mean that the ring covers only a fraction of each pixel. Because the data were calibrated as though each pixel were fully illuminated, we must correct for this fractional filling of the pixels to derive an accurate normalized reflectance for the ring. Dividing the stated reflectance values by this "filling factor," f, where

$$f = \frac{A_{\text{ring}}}{A_{\text{pixel}}} = \frac{A_{\text{ring}}}{d^2 \phi_x \phi_y / \mu}, \qquad (3)$$

we can determine the ring's actual reflectance. Here A_{pixel} is the area of the NIMS pixel projected onto the ring plane. A_{ring} is the area of the ring within the pixel footprint. The distance to the ring is given by d. ϕ_x and ϕ_y represent the angular resolution of the pixel in the cone and cross-cone directions, respectively. We assume that the values we obtained from the NIMS data represent the ring's average brightness and use these values in our analysis. This has the effect of sampling the ring's brightness at different ring radii unevenly (see, for example, Showalter et al., 1987, Fig. 4.9). The systematic error thus introduced should be small, especially far from the ring ansa. And, because this will represent only an overall increase or decrease in the ring's brightness and not change the shape of the spectra we model, the implications for our results are minimal, even at location A where such effects should be most significant.

As described in McMuldroch et al. (2000), the relatively low signal-to-noise ratio in the C3 data cube presents some difficulties in the analysis of these data. The ranges of the 17 detectors do not overlap and slight differences in the absolute calibration of each detector lead to discontinuities across detector boundaries. In higher signal-to-noise obser-
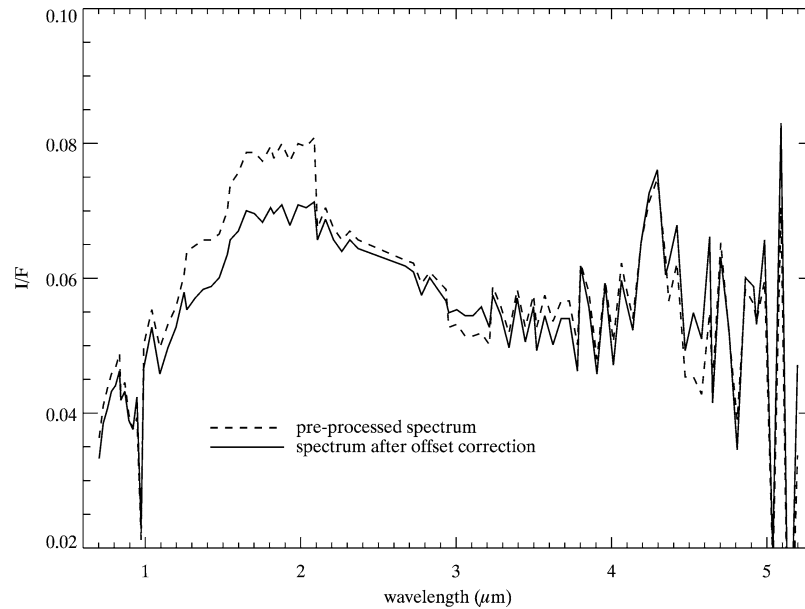
Fig. 6. Spectrum B before and after the offset correction has been applied. The most obvious discrepancy at 2.1 μm is largely eliminated after the process. Additionally, any artifacts introduced by this process are negligible.
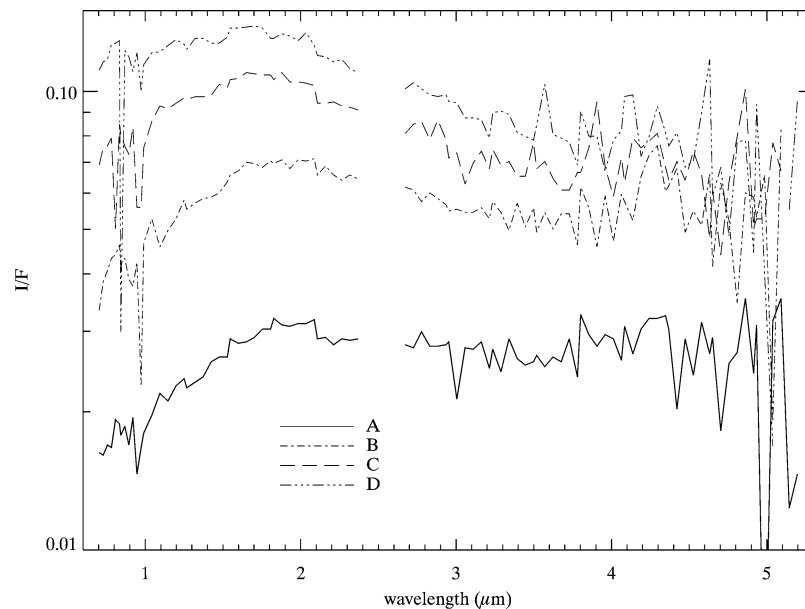

Fig. 7. The spectra of the jovian main ring taken from NIMS cube C3R0001 are plotted. Under-filling of the pixels has been taken into account (i.e., spectra have been adjusted by the appropriate value for f). The letters correspond to positions along the ring from which the data were taken. The spectra labeled A, B, C, and D were taken from pixels whose lines of sight passed 1.72, 1.61, 1.43, and 1.24R_J from Jupiter, respectively. The small discontinuities just longward of 2 μm may represent remnants of the larger discontinuities from the pre-processed data.

vations, these differences are negligible. But, in the case of the C3 ring observation, these differences are comparable to the noise level in the data. Some regions of the cube which should contain only empty sky show non-zero normalized reflectance values. In order to correct for these detector offsets, we subtracted spectra from regions of the cube that should have shown only empty sky from our ring spectra. A small region of "empty sky" pixels adjacent to our locations A, B, C, and D were averaged together at each wavelength.

The empty sky spectra were then subtracted from the corresponding ring spectra to make the detector offset correction.

This process is similar to that performed by McMuldroch et al. (2000). Figure 6 shows the spectrum taken from location B before and after the correction was made. In each of the four spectra, the differences are most significant between 1 and 2 μm. The four processed spectra are shown in Fig. 7.

Noise levels in the data were estimated by summing the standard deviation of the ring pixels and that of the
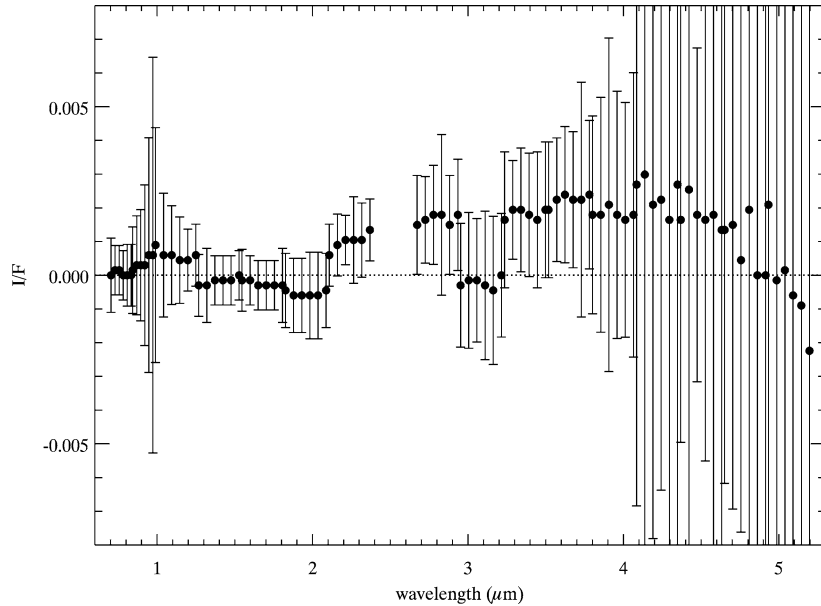
Fig. 8. The E4 observation of the main ring failed to yield a clear detection. Viewed at a phase angle of 152°, the main ring was below the NIMS detection limit.

empty sky pixels in quadrature at each wavelength (i.e., $\delta_N \approx \sqrt{\sigma_{\text{ring}}^2 + \sigma_{\text{empty sky}}^2}$, where δ_N is the estimated noise level). With the exception of some particularly noisy data around 1 micron, the noise levels in the processed spectra are generally $\sim 20\%$ of the ring signal shortward of 3.6 μm. At location A, the signal-to-noise levels are lowest and $\sim 10 : 1$ between 1.2 and 2.7 μm. These numbers are comparable to those given in McMuldroch et al. (2000). In each spectrum, noise levels increase significantly beyond 3.81 μm. Structure associated with the detector offsets are mostly eliminated by our subtraction of the "empty sky" spectra. However, it appears that this correction may not have totally eliminated the offset seen at ~ 2 μm in all of the spectra. In any event, the small discrepancies that remain are consistent with the size of our error bars.

The ring's brightness peaks at ~ 2 μm in each spectrum. At higher phase angles, this peak tends to come at shorter wavelengths. Shortward of this peak, the spectra are generally red, but with varying slopes. Between ~ 2 and ~ 4 μm, however, the NIMS spectra are all flat or slightly blue, with a trend towards bluer spectra as one moves outward from the planet from location D to A and towards lower phase angles. Beyond ~ 4 μm, the very low signal-to-noise ratios preclude any definitive statements on the character of the spectra.

3.2.2. E4 NIMS data

Because there is no clear signal from the ring at any wavelength in the E4 data, we produced a spectrum to use as an upper limit for the ring's brightness by averaging over each pixel at a given wavelength.

These data are shown in Fig. 8. The error bars in the spectra represent 1-σ deviations from the average I/F at that wavelength. The observation covers a region of space

roughly 2300 km ($0.03\,R_J$) across along the ring plane. Pointing uncertainties for this observation should be $\leqslant 0.2$ mrad (0.01°) (Lucas Kamp, personal communication, 2000). As the observation covers a field of view roughly 10 mrad in the direction orthogonal to the ring plane, it is unlikely that the lack of any ring signal is simply the result of aberrant pointing.

4. Modeling

4.1. Mie theory

The way in which a particle scatters incident light depends upon its physical properties, including its size, shape, index of refraction, surface roughness and porosity. Light-scattering measurements, therefore, can be used to infer such physical properties. Early last century Gustav Mie considered the specific case of a uniform, spherical, dielectric particle. Maxwell's equations, as applied to the interaction between such a particle and an incoming light wave of a given wavelength at distances sufficiently far from the particle, can be written explicitly and solved (van de Hulst, 1957; Hansen and Travis, 1974; Bohren and Huffman, 1983). The solution is a function only of the particle's complex index of refraction, $n_c = n_r - i n_i$, where n_r and n_i refer to the real and imaginary components of the refraction index, respectively, and its size parameter, $x \equiv 2\pi r/\lambda$, where r is the particle's radius and λ is the wavelength of the incident light. In this work we use Mie theory to predict the scattering behavior of ring particles in the tenths to tens of microns size range.

From analyses of Galileo and Voyager observations made at high phase angles (Grün et al., 1980; Jewitt and Daniel-
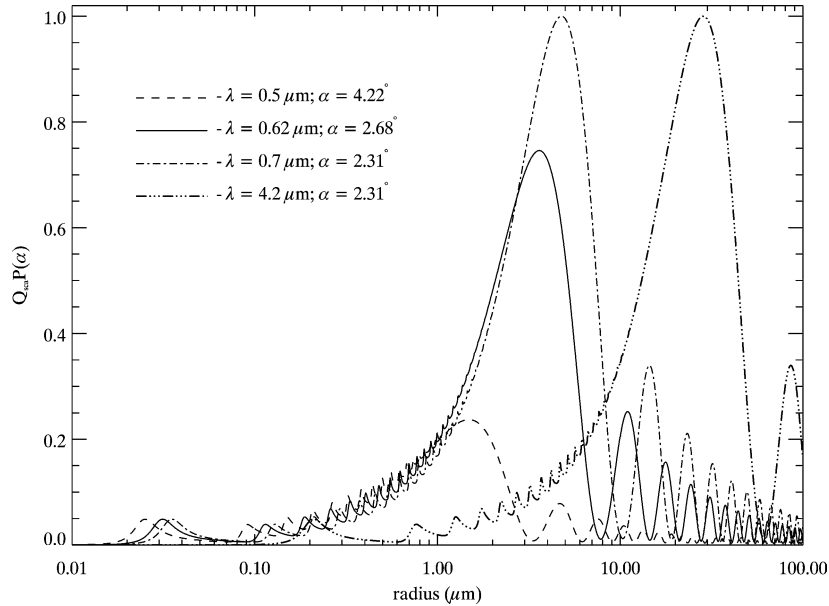
Fig. 9. The relative contribution to the total scattered light as a function of particle size. The four curves correspond to the wavelengths and scattering angles of the Voyager ISS (0.5 μm), Galileo SSI (0.62 μm), and NIMS (0.7 μm, 4.2 μm) observations. This plot shows how the brightness of the ring at the Voyager ISS wavelengths and phase angles is dominated by particles around 1 μm in size. The Galileo SSI and NIMS observations were taken at wavelengths and phase angles that probe the ring particle distribution at larger sizes. The Galileo data, especially the NIMS data, are sensitive to portions of the particle distribution that are not well described by a single power law. Because particles below about 0.1 μm do not scatter very effectively at these wavelengths, the size distributions derived from the analyses of these data cannot be reliably extended down to particles of that size and smaller.

son, 1981; Showalter et al., 1987; McMuldroch et al., 2000), the main ring is thought to contain a significant population of micron-sized particles. Observations taken at forward-scattering angles (i.e., $\theta \sim 0°$) tend to emphasize the particles in the distribution whose sizes are comparable to the wavelength of the observation. This is due to the fact that diffraction dominates the scattering behavior at small scattering angles. The half angle of the diffraction lobe is $\sim \pi/x$. Thus, it is particles with a radius

$$r \sim \lambda/2\theta_{\text{obs}} \tag{4}$$

that preferentially scatter light into the viewing angle of the observer (see also Cuzzi et al., 1984; Burns et al., 1984).

As Fig. 9 shows, the viewing geometries of the C3 NIMS and SSI observations are such that particles in the micron- to tens of micron-size range dominate the scattering. Shown in Fig. 9 are the contributions to the observed intensity by a single particle as a function of particle size, calculated with Mie theory. Each curve corresponds to the intensity predicted for a particular scattering angle and at a particular wavelength. These have been chosen to correspond to the viewing geometries and wavelengths from the Voyager ISS, Galileo SSI and NIMS observations of interest.

Pollack and Cuzzi (1980) compared the results of light scattering experiments for a variety of scattering angles and particle shapes to the predictions of Mie theory. They concluded that the scattering behavior of real particles deviates most significantly from Mie theory at large particle sizes and for intermediate and large scattering angles. Mie theory does

provide an approximate fit to laboratory data taken at small angles of scatter (Pollack and Cuzzi, 1980). Irregularities in particle shape strongly affect scattering behavior only when those irregularities become comparable to the wavelength of the scattered light. Even for such particles, the effect is less significant at small scattering angles and for randomly oriented ensembles of particles (Pollack and Cuzzi, 1980; Showalter et al., 1987).

Following the work of Jewitt and Danielson (1981), Showalter et al. (1987), and McMuldroch et al. (2000), we chose to model the scattering behavior of the particles in Jupiter's main ring with Mie theory. As did Showalter et al. (1987) and McMuldroch et al. (2000), we have employed an index of refraction of $1.5 - i0.01$, consistent with that of the dark, lossy grains expected at Jupiter (Neugebauer et al., 1981; Burns et al., 1984). Within its diffraction lobe, a particle's scattering behavior is not particularly sensitive to the value chosen for n_c, assuming that n_i is sufficiently large (Showalter et al., 1987).

4.2. Simple power laws

To reproduce the ring's phase curve, we compute the quantities τ, ϖ_0, and P in Eq. (1) for the particles in the ring. τ and ϖ_0 are simply (see Cuzzi et al., 1984)

$$\tau(\lambda) = \int_{r_{\min}}^{r_{\max}} n(r)\pi r^2 Q_{\text{ext}}(r, \lambda) \, dr, \tag{5}$$

$$\varpi_0(\lambda) = \int\limits_{r_{\min}}^{r_{\max}} n(r)\pi r^2 Q_{\mathrm{sca}}(r,\lambda)\,dr$$

$$\times \left(\int\limits_{r_{\min}}^{r_{\max}} n(r)\pi r^2 Q_{\mathrm{ext}}(r,\lambda)\,dr \right)^{-1}, \qquad (6)$$

where $n(r)\,dr$ is the vertically-integrated number of ring particles per unit area in the size range $[r, r+dr]$. The quantities $Q_{\mathrm{ext}}(r)$, $Q_{\mathrm{sca}}(r)$, and $P(r,\theta)$ can all be calculated from Mie theory. Substituting Eqs. (5) and (6) into Eq. (1) we see that, for a distribution of particles in the single-scattering regime (i.e., $\tau/\mu \ll 1$), their normalized reflectance is related to their phase functions and scattering efficiencies as

$$4\mu \frac{I}{F} = \tau \varpi_0 P(\theta) = \int\limits_{r_{\min}}^{r_{\max}} n(r)\pi r^2 Q_{\mathrm{sca}}(r) P(r,\theta)\,dr. \qquad (7)$$

The size distributions used in our calculations extend from 0.01 up to 100 µm. The distributions were divided into 1500 logarithmically-spaced bins. At the lower end of this limit and at the phase angles of the observations we studied, the contribution from an individual Mie scatterer to the ensemble brightness goes as x^6; unless particles of this size range dominate the size distribution, they contribute very little to the ring's overall brightness. Above ~ 100 µm, $x > 1000$ for the shortest wavelength observations we model. Particles this large have diffraction lobes at such wavelengths that are much smaller than the observed scattering angles ($\lambda/2r \sim 0.18°$ at 0.6249 µm for a 100-µm particle). Thus, unless their numbers overwhelm the smaller particles, they are essentially invisible in these observations. Larger values for $r_{\max}$ and smaller values $r_{\min}$ were tried and found to not significantly affect our results.

McMuldroch et al. (2000) discretized Eq. (7) and iteratively solved it to obtain $n(r)$ from the NIMS data. Because of the inherent difficulty of inverting data with noise levels as high as those in the NIMS data (Menke, 1984), we have chosen a forward-modeling approach in which the general form of a size distribution is assumed. Equation (7) is then used to calculate brightness as a function of wavelength and phase angle that is compared to the photometric and spectroscopic measurements. Best fits were determined by minimizing the fit residuals to the data. We first considered a differential power law distribution for the ring particles such that

$$n(r)\,dr = C(r/r_0)^{-q}\,dr, \qquad (8)$$

where q is the power law, or spectral, index and r_0 is a reference size taken to be 1 µm. This choice was motivated by several factors. Power laws have the advantage of being simple. The size distributions of the debris resulting from ring material-producing collisions are usually described by power laws (Greenberg et al., 1978; Grün et al., 1980). And, because collisions are thought to be an integral part of the creation and evolution of planetary ring systems, modeling the ring particle distribution as a power

law makes our results directly applicable to evolutionary and dynamical ring models. Finally, because other photometric models (Grün et al., 1980; Showalter et al., 1987; McMuldroch et al., 2000) have employed power law size distributions, we can compare our derived distributions to previous results.

By predicting the particle brightness at the observed scattering angles via Eq. (7), one can derive a best fit to C and q from a phase curve. Showalter et al. (1987) analyzed the Voyager phase curve derived from high phase angle images and found a power-law index, $q = 2.5 \pm 0.5$. Using Eq. (2) and the brightness of the ring as viewed through Voyager's orange and violet filters, they found that $q = 2.2 \pm 0.2$. For C, Showalter et al. (1987) determined values of: $C = 0.98 \pm 0.13$ cm^{-2}/µm for $q = 2.0$; $C = 1.71 \pm 0.10$ cm^{-2}/µm for $q = 2.5$; $C = 2.12 \pm 0.07$ cm^{-2}/µm for $q = 3.0$. (The units cited here are slightly different than those in Showalter et al. (1987) because of our inclusion of the factor $(1/r_0)^{-q}$ in Eq. (8); the units above are consistent with our definition for the power law distribution.) Values for the ring's optical depth corresponding to these distributions range from 1–6×10^{-6}.

Our analysis shows that the Galileo SSI phase curve is best fit for $q \leqslant 2.3$. For $q < 2$, the ensemble scattering behavior is dominated by the larger particles in the distribution. The phase curves of such size distributions are generally insensitive to q and do not constrain that parameter well. The values that Showalter et al. (1987) determined for q are consistent with this result. Our derived value for C is 1.12 ± 0.13 cm^{-2}/µm for $q = 2.0$. For such a distribution $\tau = 7.2 \times 10^{-6}$.

As we did with the Galileo SSI phase curve and Showalter et al. (1987) did with the phase curve from Voyager ISS data, McMuldroch et al. (2000) analyzed phase curves derived from the Galileo NIMS data. They modeled the ring's phase behavior at 20 of the data set's 96 wavelengths. Claiming that noise levels in the data at wavelengths less than 1.0 µm and greater than 4.0 µm precluded any meaningful, quantitative use, McMuldroch et al. (2000) chose to exclude them from their analysis. A drawback to their approach is that the phase coverage within the C3 NIMS data set is relatively limited. For this observation, the phase angle varies just 0.8° from 177.6° up to 178.4°, which differs from that reported by McMuldroch et al. (2000). This is because the geometry information initially released with this NIMS observation did not contain the phase angle between the line of sight to the rings and the line connecting the Sun and the location where the ring plane and line of sight intersect, which is the appropriate angle for this analysis. Instead, the geometry information initially released contained the phase angles of the observation points *projected onto Jupiter*, which is what McMuldroch et al. used. This was subsequently corrected in results made available to us by Lucas Kamp at JPL.

Our approach to modeling the NIMS data was to vary λ, as opposed to the phase angle, and model the ring spectra. As with the SSI data, we used a power law to describe the

ring particles' size distribution. We also assumed that n_c is not a strong function of wavelength. That no obvious spectral features are apparent in the data suggests that this is a reasonable assumption. Because location A is furthest from the planet, these pixels should contain the smallest contributions from scattered light and the halo. We derived best-fit values for q of 2.6 ± 0.3 from our analysis of this particular spectrum, which compares well to the value Showalter et al. (1987) derived from the Voyager phase curve. At location B we derive a similar best fit of 2.7 ± 0.4. The best fit at location C has $q = 2.9 \pm 0.4$. And, from location D we derive a best fit of $q = 3.1 \pm 0.3$. These results and those from fits to the E4 observation are summarized in Table 3.

To provide another measure by which to compare the NIMS results with the SSI and Voyager results, we used our derived size distributions to predict the normal optical depth of the main ring at $0.62\,\mu m$. Assuming that the particles are Mie scatterers, the E4 data provide the constraint that $\tau \leqslant 6.8 \times 10^{-5}$ at $0.62\,\mu m$. Jewitt and Danielson (1981) used high phase angle Voyager images and assumed a value of 0.04 for the ring's albedo to derive a value for τ of 3×10^{-5}. The size distributions inferred from modeling the C3 NIMS data yield optical depths that lie between the values determined by Jewitt and Danielson (1981) and Showalter et al. (1987).

4.3. Broken or two-component power laws

As shown in Fig. 10, even the best fits to the four NIMS spectra generated with the single power law size distributions (dashed lines) only crudely reproduce the features of these spectra.

At these scattering angles, distributions which span the size range we consider and which are characterized by power law indices with $q > 3$ yield spectra that are blue, especially at shorter wavelengths. Spectra produced with a q of 3 are flat. The predicted spectra from power law distributions shallower than 3 are red. The NIMS spectra we modeled show a red *and* a flat or slightly bluish trend depending upon the wavelength under consideration (see Fig. 7).

Our initial approach to dealing with the discontinuities in the NIMS spectra was to model the spectra piece-by-piece, analyzing the data from each detector separately. The size distribution was assumed to be a power law. The detector offsets would have produced an uncertainty in the absolute amount of ring material, but would not have affected the shape of the size distribution. Therefore, we expected to obtain 16 independent, yet comparable, determinations of the size distribution's power law index.

Table 3
Power law fits to NIMS spectra

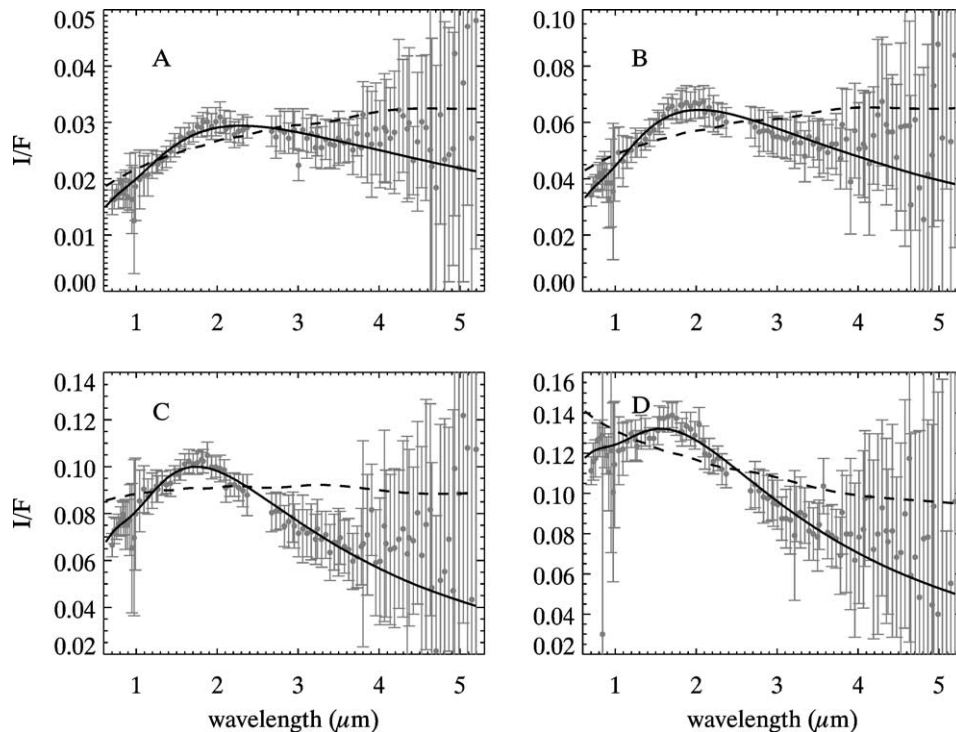| Spectrum ID	q	$\tau_\lambda = 0.6249\,\mu m$ (10^{-6})
A	2.6 ± 0.3	7.1–8.1
B	2.7 ± 0.4	13–17
C	2.9 ± 0.4	16–30
D	3.1 ± 0.3	18–45
E4	...	< 68

Fig. 10. The data from spectra A, B, C, and D are plotted against our best fit models to the data. The dashed lines represent the best fit simple power laws; the best fit broken power laws are plotted with a solid line. In each case, the broken power law model clearly produces a better fit to the spectrum.
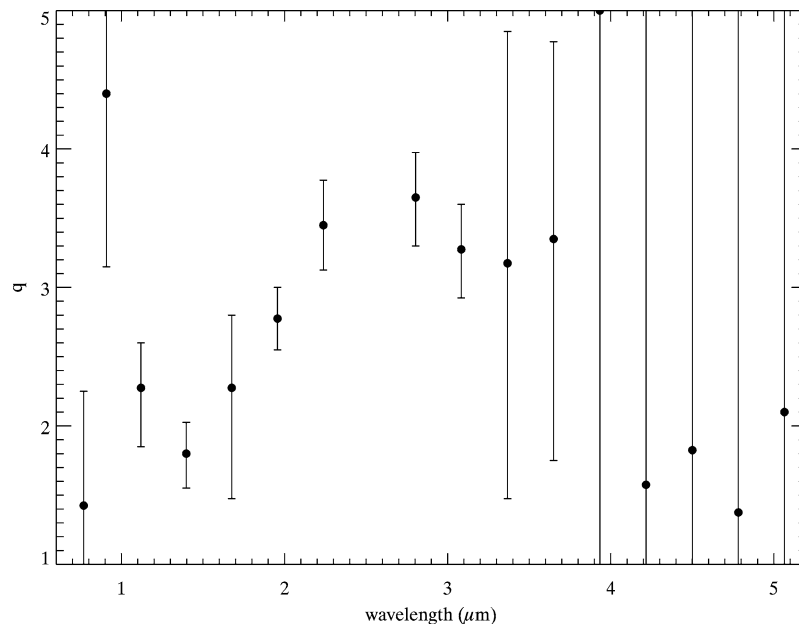
Fig. 11. Attempting to circumvent the difficulties posed by the calibration differences between the 17 NIMS detectors, we produced photometric models of the ring's size distribution by fitting them separately to data derived from each detector. The distribution was assumed to be a power law, the index of which was allowed to vary between 1.0 and 5.0. Best-fit power law indices fit to spectrum B are shown as a function of wavelength. Below $\sim 2\,\mu$m, the best fits are, with one exception, less than 2.9 and generally increase with wavelength. Beyond 3.9 μm, the data are too noisy to constrain the model. Aside from those data, the best fits are consistently above 3.2 longward of $\sim 2\,\mu$m. McMuldroch et al. did not fit data shortward of 1 μm and beyond 4 μm because of the large errors bars on these data.

The results are shown in Fig. 11. Instead of the fits clustering around one value, we found that at wavelengths less than 2 μm the preferred power law index is below 3. However, beyond 2 μm, the fits abruptly switch to values larger than 3. Above 3.9 μm, the data do not constrain q well. Because the majority of the signal observed by NIMS at these scattering angles is diffracted light, the size of the particles primarily responsible for the ring's brightness at a given wavelength varies as described by Eq. (4). Thus, as shown in Fig. 9, the intensity observed at the shorter NIMS wavelengths samples the size distribution at smaller particle sizes than do observations at longer wavelengths. Combined with our detector-by-detector results, the abrupt change in power law index suggests that a more complex size distribution is required.

Such photometric models for the NIMS spectra suggest that the power law index describing the small end of the size distribution is different than the index for the larger particles. To capture this behavior, we elected to employ a *broken* or *two-component* power law. For such a distribution,

$$n(r)\,dr = \begin{cases} C_1 (r/r_0)^{-q}\,dr & \text{for } r \leqslant r_{\text{brk}}, \\ C_2 (r/r_0)^{-(q+\delta q)}\,dr & \text{for } r \geqslant r_{\text{brk}}, \end{cases} \quad (9)$$

where r_{brk} is the particle size at which the size distribution switches over to a new spectral index. A value of 1 μm was chosen for r_0. C_1 and C_2 can be related to one another through the condition that the size distribution be continuous at $r = r_{\text{brk}}$, i.e.,

$$C_2 = C_1 \left(\frac{r_{\text{brk}}}{r_0} \right)^{\delta q}. \quad (10)$$

(Note: we have kept $r_0 = 1\,\mu$m for consistency, but the mathematical description of this distribution can be simplified and Eq. (10) can be eliminated by setting $r_0 = r_{\text{brk}}$.)

As with the simple power law distribution, such a size distribution is likely an oversimplification of the actual size distribution. However, this broken power law distribution retains many of the same advantages as does the simple power law. Its mathematical description is still relatively simple. And, its relevance to other photometric and evolutionary models is fairly straightforward. Similar size distributions have been suggested for other planetary rings. Marouf et al. (1983) determined the size distributions in portions of Saturn's A and C rings and in the Cassini division from Voyager 1 radio occultation data. The size distribution they derived in the meter-size range can also be described as a broken power law.

The best fits derived using the broken power law size distributions reproduce the NIMS spectra significantly better than do the best fits from the power law size distributions. Figure 10 shows these best fit spectra plotted against each of the NIMS spectra. Broken power laws have twice the number of free parameters than do simple power laws. Although this extra flexibility does, in part, explain the improved fits, the detector-by-detector results provide evidence that the shape of the distribution *does* change over the particle size range considered. We considered distributions such that $r_{\text{min}} = 0.01\,\mu$m and $r_{\text{max}} = 100\,\mu$m. r_{brk} was allowed to vary between 5.0 and 30.0 μm. q was varied between 0.0 and 3.0 and values from 1.0 up to 7.5 were used for δq. With the exception of δq, for which we could only deter-

mine lower limits in spectra C and D, these ranges encompass the values which provide an acceptable fit to the NIMS data.

The slope of the short wavelength end of the spectra dictates the best fit values for q, whereas δq is constrained by the slope of the spectra at longer wavelengths. The value of r_{brk} controls where the predicted spectra switch slope; larger values of r_{brk} cause this switch to occur at longer wavelengths. Table 4 summarizes our fits to the NIMS data. In reality, the solution space is somewhat more complex than Table 4 suggests. Many of the values we tried for r_{brk} can be used to fit the spectra. There is a rough correlation between r_{brk} and δq. Larger values for r_{brk} generally require higher values for δq to satisfactorily match the ring spectra; a value of δq from Table 4 that fits a particular spectrum well for a given value of r_{brk} may not fit the spectrum for larger values of r_{brk}, even within the size ranges given. Of these parameters, q is best constrained. The results from the fit to spectra A and B suggest that below a size of $\sim 15\,\mu m$ the particles in the main ring follow a power law distribution with an index of 2.0 ± 0.3; between ~ 15 and $100\,\mu m$, the distribution steepens such that $q + \delta q \simeq 5.0 \pm 1.5$.

Table 4
Two-component power law fits to NIMS spectra

Spectrum ID	q	r_{brk} (μm)	δq	$\tau_{\lambda=0.6249\,\mu m}$ (10^{-6})
A	2.0 ± 0.3	14.5 ± 3.5	2.5 ± 0.9	3.6–5.5
B	2.0 ± 0.3	16.0 ± 3.5	3.5 ± 1.1	6.5–9.2
C	2.3 ± 0.2	18.0 ± 3.5	> 2.5	8.6–12
D	2.6 ± 0.2	22.0 ± 4.0	> 2.0	8.8–19

The spectrum of a broken power law distribution of particles exhibits a distinctly different behavior than does that from a distribution following a regular power law. Figure 12 shows two spectra, at the phase angles from spectrum A and spectrum D, for an ensemble of particles described by a power law size distribution and that of an ensemble following a broken power law, as calculated using Mie theory. The power law distributions look very similar when viewed at different phase angles. This is because, although particles of different sizes are being highlighted at different phase angles, the shape of this distribution is everywhere the same for an infinite range of sizes. (As the size range of a real or simulated distribution must be finite, this will not be strictly true in practice.) The broken power law distribution, however, does *not* look the same at all phase angles. The distribution changes shape at r_{brk} and the degree to which particles above and below this size scatter light towards the observer depends upon the observer's viewing angle (see Eq. (4)). The phase behavior of the broken power law distribution helps to explain some of the differences in the NIMS spectra. Specifically, the tendency of the broken power law distribution to produce a relatively flat distribution at lower phase angles and a distribution that is more peaked at $\sim 2\,\mu m$ as one moves to higher phase angles mimics most of the general characteristics of the four NIMS spectra.

We also attempted to fit the SSI phase curve with a broken power law size distribution. Naturally, the results were not as definitive as those for the NIMS data. This is because, as Fig. 9 implies, these data do not have quite as much leverage over the particle size range beyond the size at which the distribution, as derived from the NIMS data, steepens. The range of particle sizes that contribute most at the wave-
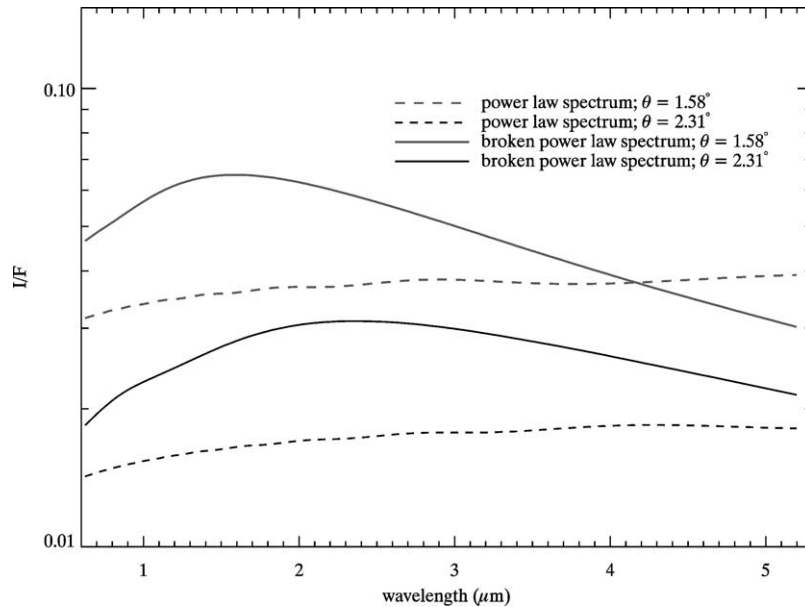

Fig. 12. The spectrum of a simple power law distribution and a broken power law distribution, as calculated with Mie theory, viewed at scattering angles of 2.31° and 1.58°, corresponding to the phase angles of NIMS spectra A and D, respectively. The distributions corresponding to each spectrum have been normalized to have an optical depth of 5×10^{-6} at $0.6249\,\mu m$. The shape of the spectrum of the power law distribution is fairly insensitive to phase. However, the differences between spectra A and D are generally consistent with the phase behavior of the broken power law distribution.

lengths and phase angles observed by Galileo are similar to those constrained by the Voyager ISS data. The SSI results suggest that $q < 2.0$, $\delta q > 1.0$, and $9.0\,\mu\mathrm{m} < r_{\mathrm{brk}} < 18.0\,\mu\mathrm{m}$. The data are consistent with a size distribution that is described by a broken power law, although the parameters describing the distribution (particularly δq and r_{brk}) are not as well constrained by the SSI phase curve as they are by the NIMS data. This is because, as Fig. 9 shows, particles larger than the value determined for r_{brk}, $\sim 15\,\mu\mathrm{m}$, do not scatter effectively at the wavelengths and phase angles of the Galileo images we analyzed.

Calculations for the normal optical depths for these distributions range from 3×10^{-6} up to 2×10^{-5}. Values for τ obtained using the broken power law fits are roughly those from the simple power law fits; these are given in Table 4.

This is because there are relatively fewer large particles above r_{brk} to contribute to the overall optical depth. It should also be noted that these optical depth predictions do not suffer as much from the same dependence on the upper size cutoff which the simple power law fits with $q \leqslant 3$ do. Each of our broken power law fits to the data have a slope greater than 3 above r_{brk}. This means that the integrand in Eq. (5) *decreases* with increasing r. And, for r_{max} sufficiently larger than r_{brk}, the integral in Eq. (5) converges.

5. The "near arm/far arm" asymmetry

Both Jewitt and Danielson (1981) and Showalter et al. (1987) reported that the arm of the main ring furthest from the spacecraft was brighter than the near arm in some of the Voyager 2 clear filter images by as much as 10%. This difference is reflected in the Voyager clear filter data at scattering angles between 5° and 6°, as shown in Fig. 4 (see also Showalter et al., 1987, Fig. 4.3). This brightness asymmetry drops to zero beyond 45° from the ansa. Showalter et al. (1987) also reported an asymmetry in wide-angle orange and violet filter images of Jupiter's limb which show the arms of the main ring (FDS 20691.27, 20691.31, 20691.35, 20691.39). In the orange/violet pair of images (FDS 20691.35/.39) which show the ring's eastern ansa, the far arm is brighter than the near arm, as in the clear filter data, by about 20% in both orange and violet images. In the pair showing the other limb of the planet and the ring's western ansa (FDS 20691.27/.31), it is the near arm that is brighter by about 5% in both images (see Showalter et al., 1987, Fig. 4.4). This is reminiscent of the quadrant asymmetry seen at Saturn (Thompson et al., 1981; Cuzzi et al., 1984), but it should be noted that the difference between the arms seen in image pair FDS 20691.27/.31 is comparable to the error bars of the measurements taken from these images. And, Showalter et al. (1987) suggest that the data taken from image pair FDS 20691.35/.39 may suffer from scaling uncertainties and variability in the vidicon response.

Ockert-Bell et al. (1999) also reported a near arm/far arm brightness asymmetry in the Galileo images. We have confirmed the existence of this asymmetry. Image sequence C3_RINGS02 (images s0368974113, s0368974126, and s0368974139) shows the ring's western ansa. The contrast is apparent even without the removal of the halo signal.
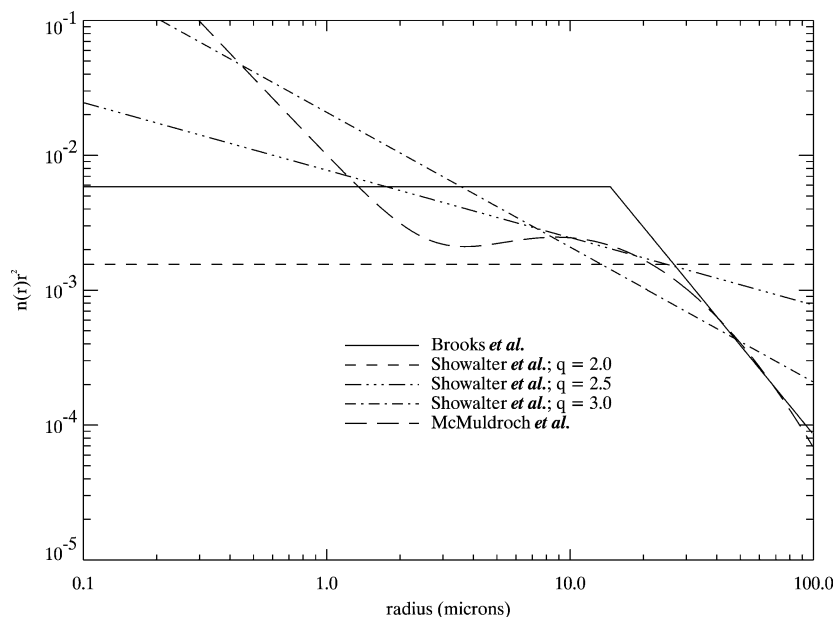

Fig. 13. The various distributions that have been derived from photometric models of the jovian main ring are shown above. They have all been normalized to the same optical depth. The lines represent the cross-sectional area (in cm^2) each distribution contains per unit ring area (also in cm^2) per size interval (in cm) as a function of particle size. Fits derived from the Galileo NIMS data, ours and those of McMuldroch et al., suggest that there is a rollover in the distribution at a size of about 15 microns. Our fits from the NIMS data, however, also agree with fits derived by Showalter et al. (1987) in the micron and sub-micron size range, which the Voyager data best constrain, as well as our own results using the Galileo SSI images.
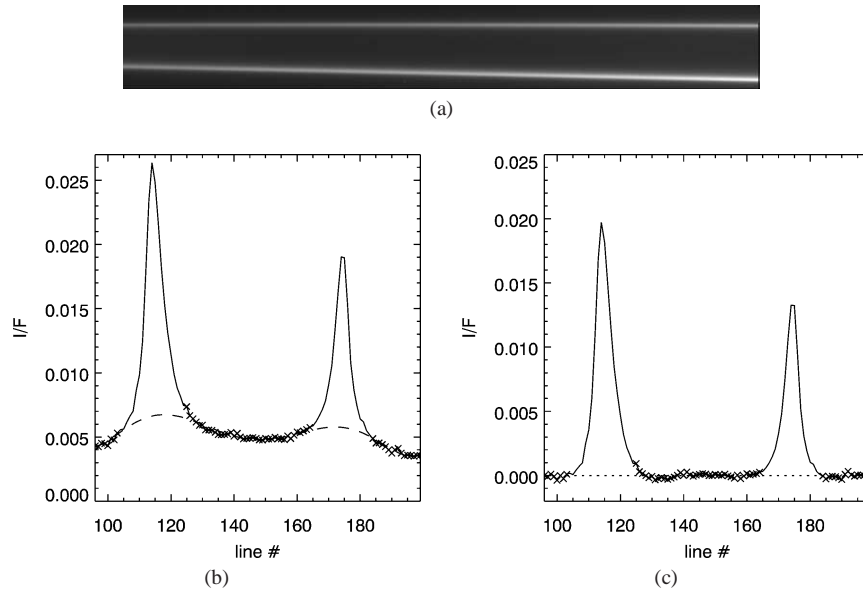
Fig. 14. The top panel, Galileo SSI image s0368974113, shows the ring arms on the western side of the planet as seen from Galileo while the spacecraft was in Jupiter's shadow. The halo signal has not been removed from this image. North is up and Jupiter is off to the right of this frame. The near arm of the ring (bottom) is noticeably brighter than the far arm (top). (b) and (c) are analogous to Figs. 2b and 2c and show the ring brightness along cuts taken through the center of the image in (a). It is clear that one arm of the ring is brighter than the other both before and after the halo has been removed. This asymmetry is also visible in Fig. 2, although the contrast between the ring arms is not as great.

Figure 14 shows Galileo image s0368974113, in which the difference in brightness between the near and the far arm is clearly visible and increases as the limb of Jupiter is approached. However, the sense of the asymmetry in the Galileo images is reversed and the ring's near arm is brighter than the far one (Ockert-Bell et al., 1999). The near arm/far arm asymmetry is reflected in the Galileo data for $\theta < 2.5°$ (see Fig. 4). Of the two data points taken at $\theta = 1.7°$, one is brighter than the other by about $60 \pm 15\%$ after the background subtraction. And, whereas the asymmetry increases *towards* the ansa in the Voyager data, we see an increase in the asymmetry with increasing distance *away from* the ansa in the Galileo SSI data. The data points at $\theta = 1.7°$ correspond to longitudes roughly $\pm 40°$ away from the ring ansa. Within $\sim 5°$ of the ansa, the asymmetry is within our error bars. Such an asymmetry is not seen in the images we analyzed from sequence C3_RNGHALO (images s0368975900, s0368975922, s0368975945), which show the eastern ansa of the ring and were obtained 18 minutes after the images in sequence C3_RINGS02. Searches for such asymmetries in the Cassini ISS images of the ring have proved unfruitful due to the significant scattered light present in these images (Throop and Porco, 2001).

This asymmetry is distinct from the small scale patches depicted in Fig. 1. The patches extend 500–1000 km in radius (Ockert-Bell et al., 1999) and just a few degrees in longitude. They exhibit no preference for any particular ring longitude (Ockert-Bell et al., 1999). The brightness variations represented by the patches do not approach the $60 \pm 15\%$ seen in the larger asymmetry. Thus, the data do not support the idea that the broader asymmetry is merely an unresolved grouping of smaller scale patches occupying

a restricted range of longitudes. Rather than being some systematic variation in brightness with ring longitude, such as the quadrant asymmetry in Saturn's A Ring, it appears that the asymmetry seen in Galileo images of the main ring is an enhancement in the ring's brightness along an arc that extends several tens of degrees in longitude.

5.1. Explaining the asymmetry

5.1.1. Photometric behavior

Voyager was typically 2° *below* the ring plane as it imaged the ring. Ockert-Bell et al. (1999) note that Galileo was typically 0.5° *above* the ring plane and suggest that this may be related to the asymmetry. However, the ring is optically thin and its integrated intensity does not depend on opening angle.

Another idea is that the observed asymmetry may arise from elongated ring particles, oriented along a particular axis, presenting cross-sections that depend upon the observer's viewing angle. It has been suggested that such an alignment of the ring particles could be created by Jupiter's magnetic field (Showalter et al., 1987). In an attempt to correlate these brightness asymmetries with the structure of the magnetic field, we have plotted the brightness of the ring as a function of System III longitude, a longitude system that is tied to Jupiter's magnetic field.

The results are shown in Fig. 15. If the asymmetry is related to the magnetic field, one might expect to see periodicities in the ring's brightness as a function of magnetic longitude. One might also expect to see brightness peaks at longitudes associated with the magnetic poles or longitudes at which the magnetic equator crosses the ring plane. No
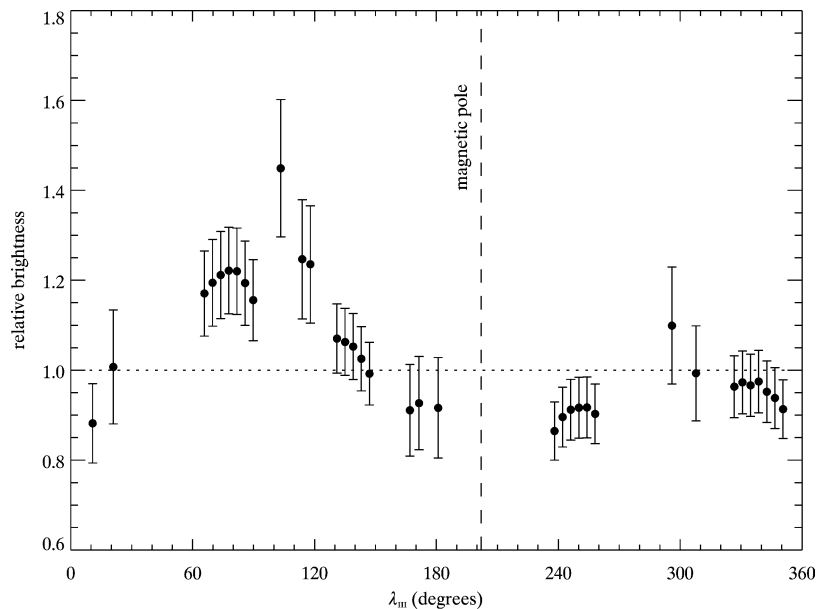
Fig. 15. The Galileo data points from Fig. 4 have been plotted as function of magnetic longitude. To account for the ring's phase behavior, the data points have been normalized by the predicted phase curve for a power law size distribution of particles with $q = 2.0$. There are no obvious patterns that would suggest a relationship with the planet's magnetic field. The peak in the Voyager clear filter data was seen at $\sim 20°$ in System III longitude.

such suggestive features were found. The magnetic pole is tilted towards $\sim 202°$ in System III longitude. After taking phase angle effects into account, we found that the brightest section of the ring, corresponding to the brighter of the two data points at $\theta = 1.7°$, lies at $103°$. No other data were taken at this same magnetic longitude by Galileo. The Voyager images highlighting the asymmetry were taken when the ansa was located $\sim 180°$ from the magnetic pole, or at $\sim 20°$ in System III longitude (Showalter et al., 1987). And, although the trend at $\sim 280°$ is suggestive of a pattern, the size of the error bars precludes any conclusions on the existence of such a pattern.

Even so, explaining the brightness differences by variations in the orientation of aligned, non-spherical ring particles is problematic. This would require a difference of some 60% in the particle phase function due to differences in orientation alone. According to Pollack and Cuzzi (1980), the phase function for non-spherical particles at scattering angles $\leqslant 60°$ is similar to that for spherical particles. As a result, the scattering properties of non-spherical particles at different orientations should be similar when viewed at small scattering angles. We cannot draw any clear association between the structure of the jovian magnetic field and the observed longitudinal brightness asymmetries. This all suggests that the near arm/far arm symmetry is a localized enhancement in the number of ring particles and not some photometric effect related to the observing geometry or ring grain orientation.

5.1.2. Impacts into ring parent bodies

Another explanation advanced by Showalter et al. (1987) for the asymmetry is the generation of debris from an impact into a ring parent body by an external impactor. Showalter

(1998) put forth a similar model for the transient "burst events" seen in Saturn's F ring. Several lines of evidence indicate the existence of such macroscopic parent bodies within the ring. Evolutionary models of the smallest ring particles suggest they are lost so rapidly from the system that larger bodies must be present to replace the dust grains that are seen (Horányi and Cravens, 1996; Burns et al., 1999). The Pioneer 11 charged particle signatures require the presence of large bodies as well (Fillius et al., 1975; Acuña and Ness, 1976). Finally, the different radial profiles the ring presents when viewed at varying phase angles implies that large ring particles exist alongside much smaller ring grains (Showalter et al., 1987; de Pater et al., 1999; Burns et al., 2004).

If the asymmetry seen by Voyager was the result of an impact into a ring parent body, the enhancement in the number of particles at a particular longitude should have sheared out in a just a few years and, as pointed out by Ockert-Bell et al. (1999), the Voyager event could not now be responsible for the asymmetry observed by Galileo. An impact origin for this asymmetry requires a more recent material-producing impact. It is difficult to precisely determine the amount of material required to produce the asymmetry seen in the Galileo images. Sequence C3_RINGS01, a series of images of the western side of the rings, ends at the limb of Jupiter. The C3_RNGHALO images show no asymmetry on the eastern side of the rings. Therefore, it is difficult to constrain the asymmetry beyond the point where Jupiter's shadow cuts off the main ring. If the ring's brightness were to increase linearly from the ansa to the location where the 60% difference in brightness between the near and far arms is observed and then immediately drop back to its nominal brightness, the extra material would represent a $\sim 7.5\%$ en-

hancement in the ring's total cross-section. If instead there were to be a symmetric decrease in brightness beyond the limb, this figure would double. We assume a value of 10%, which is sufficient for the discussion that follows. Showalter et al. (1987) determined that the asymmetry seen in the Voyager data represents an extra $\sim 1\%$ of ring material.

Assuming that collisional ejecta follow the size distribution of Grün et al. (1980) and that the ring grains have a density somewhere between 1–3 g/cm^3, an extra $\sim 10\%$ optical depth in dust grains represents $\sim 10^9$–10^{10} g of material. The mass of the ejecta generated in an impact, m_{ej}, can be related to the mass of the impactor, m_{imp}, through the parameterization of Greenberg et al. (1978):

$$m_{ej} = \frac{1}{2} m_{imp} v_{imp}^2 k_{ej}, \tag{11}$$

where k_{ej}, the ejecta yield, has a value of $\sim 2 \times 10^{-8}$ g/erg for unbonded quartz sand and $\sim 1.5 \times 10^{-9}$ g/erg for weakly bonded quartz sand (Greenberg et al., 1978). The precise velocity of a given impact will depend upon the geometry of the impact. A prograde impactor approaching from infinity and impacting Metis' trailing side will hit at a velocity, $v_{imp} = (\sqrt{2} - 1) v_{orb} = 13$ km/s, where v_{orb} is Metis' orbital velocity about Jupiter of 31.55 km/s. This neglects both Jupiter's motion about the Sun and the impactor velocity at infinity, which are small relative to Metis' orbital velocity. For a retrograde impactor striking Metis' leading side, $v_{imp} = (\sqrt{2} + 1) v_{orb} = 76$ km/s. Using a Monte Carlo algorithm, Zahnle et al. (2003) have determined the average cometary impact velocity onto Metis velocity to be 59 km/s. Allowing for these ranges of k_{ej} and v_{imp} and assuming that all of the impact ejecta escapes the target, the mass of the impactor needed to produce the required amount of material is $\sim 10^4$–10^7 g. This corresponds to an impactor with a diameter of ~ 10–100 cm. Slower impact velocities require a larger impactor to produce the same amount of ejecta and vice versa.

Impacts into one of the main ring parent bodies should occur at a rate

$$v_{ring} = \frac{A_{ring} \tau_{pb}}{A_{\jupiter}} v_{\jupiter}, \tag{12}$$

where A_{ring} and $A_{\jupiter}$ represent the areas of the main ring and that of Jupiter, respectively. $v_{\jupiter}$ is the impact rate onto Jupiter. τ_{pb} is the normal optical depth of parent bodies in the main ring. If we assume that large particles dominate the scattering at small phase angles, the optical depth of the ring as calculated from images taken at back-scatter can be used to place an upper limit on τ_{pb}. The geometric albedo, p, is defined as

$$p \equiv \frac{\varpi_0 P(\theta = 0°)}{4}. \tag{13}$$

Showalter et al. (1987) assume that large ring particles have an albedo of 0.05, similar to that of Amalthea, and use Eqs. (1) and (13) to calculate an optical depth of 3×10^{-6}. Quoting values of 0.085 and 0.12 for p, respectively,

Nicholson and Matthews (1991) calculate a value of 5×10^{-6} for τ, whereas Meier et al. (1999) find $\tau = 4 \times 10^{-6}$. Given this range of albedos, the observations of de Pater et al. (1999) are consistent with a τ between 3×10^{-6} and 1×10^{-5}. Since we are only interested in order of magnitude estimates, we adopt a value of 10^{-6} for τ_{pb}. This value is consistent with the estimate for τ_{pb} from Brooks (2003).

The product $A_{ring} \tau_{pb}$ gives the total cross-sectional area of the parent bodies in the main ring. The appropriate value to be used for A_{ring} is the area of the ring inhabited by the parent bodies. However, values typically quoted for the ring's inner and outer radii (Showalter et al., 1987; Ockert-Bell et al., 1999) are derived from forward-scatter images of the ring, in which the parent bodies are generally invisible. Meier et al. (1999) fit model cross-sections to profiles derived from their low-phase NICMOS images of the ring. Their results suggest that the parent bodies are concentrated towards the outer edge of the main ring. Low phase Galileo SSI images of the main ring taken during orbits G28 and G29 also show that the bulk of the main ring parent bodies are concentrated in the outermost ~ 2000 km of the ring (Brooks, 2003; Burns et al., 2004).

We can use the impact rate onto Jupiter derived by Zahnle et al. (2003) to estimate the frequency of such impacts. The rate at which bodies smaller than 1.5 km impact Jupiter is, according to Zahnle et al. (2003),

$$v_{\jupiter} = 5 \times 10^{-3} \, (d/1.5\,\text{km})^{-1}/\text{year}, \tag{14}$$

where d is the diameter of the impactor. Substituting Eq. (14) into Eq. (12), the frequency with which a sufficiently large impact into a main ring parent body occurs can be calculated to be on the order of just $\sim 10^{-6}$–10^{-7} per year. Repeating this calculation for an impact large enough to produce the asymmetry seen by Voyager yields a frequency of $\sim 10^{-5}$–10^{-6} per year.

Cuzzi and Estrada (1998) provide another impactor flux which can also be used to calculate an impact rate. They constrain the impactor flux in the outer Solar System with an evolutionary model of Saturn's rings. Their flux is consistent with Pioneer 10, Pioneer 11, and Ulysses measurements. Showalter (1998) uses the Cuzzi and Estrada flux to come up with a flux of $10^{-18\pm1.5}$ m^{-2}/s for impactors ~ 10 cm in size. Showalter then multiplies this by a gravitational focusing factor of 3 to 30. With this flux, Showalter creates a model for the origin of the three "burst events" in Saturn's F Ring observed by Voyager. Performing the same exercise at Jupiter yields a focusing factor of ~ 100, depending on the velocity with which impactors are assumed to approach the planet, and a frequency of impacts into the main ring parent bodies of anywhere between 0.3–300 such impacts per year.

Extending either of the impactor flux models used by Cuzzi and Estrada and Zahnle et al. to the 10–100 cm size range is a significant extrapolation. Such extrapolations are necessary because the size distribution of impactors in the jovian system in this size range is very poorly constrained.

Observational evidence does exist, however, to suggest that the number of impactors of this size is small. Bierhaus et al. (2001) investigated the crater population on Europa from 0.05 to 1 km in diameter. From Eq. (2) in Zahnle et al. (2003), impactors of the size necessary to produce the ring asymmetry should produce craters just below the range of crater sizes examined by Bierhaus et al. (2001). Bierhaus et al. conclude that a large fraction of the number of small craters ($\leqslant 1$ km in diameter) can be accounted for by secondary cratering from the few large impacts (> 10 km) seen on Europa. This, in turn, implies that the number of centimeter- to meter-sized primary impactors is smaller than the cratering record might otherwise suggest.

5.1.3. Impacts between ring parent bodies

Another mechanism that may be responsible is that outlined in Cuzzi and Burns (1988) to explain some of the charged particle depletions detected by Pioneer 11 in the vicinity of the F ring. In their model, Cuzzi and Burns attribute the observed charged particle depletions that cannot be explained by the presence of the F ring, Prometheus or Pandora to absorption by low optical depth (10^{-3}–10^{-4}) clouds of material released when larger, unseen parent bodies collide. The clouds of material spread longitudinally due to Keplerian shear and are eventually swept back onto the surfaces of the parent bodies, to be released in subsequent collisions. Barbara and Esposito (2002) posit a similar model to explain the "burst events" observed in the F ring. In the particle-in-a-box approximation, the time between parent body collisions is roughly

$$t_{\text{coll}} \sim \frac{1}{\Omega \tau_{\text{pb}} n_{\text{pb}}}, \qquad (15)$$

where Ω is the orbital frequency at the ring's distance from Jupiter, n_{pb} is the number of parent bodies and τ_{pb} is their optical depth. Assuming a mono-modal parent body size distribution, n_{pb} and the collision frequency between those parent bodies can be estimated.

Table 5 summarizes the results of such an exercise for a few particle sizes. For 10-m particles, collisions should be frequent, roughly 10^5 per year. About ten collisions between 1-km parent bodies would be expected to occur in a year. This also requires that particles in the ring have eccentricities sufficiently large that the particle-in-a-box approximation is reasonable.

The collision velocity required to release 10^{10} g of ejecta when two parent bodies collide should be compared to the dispersion velocity expected for parent bodies in such a ring,

which will resemble the typical impact velocity. The typical collision velocity, δv, can be estimated from the ring thickness, h, as $\delta v \sim v_{\text{c}} h / a$, where v_{c} is the local Keplerian velocity (Burns et al., 1984). Using low-phase angle Voyager images, Showalter et al. (1987) constrained $h \leqslant 30$ km. This yields a value of $\leqslant 10$ m/s for δv. According to Eq. (11), parent bodies in the 10–100 m size range colliding at this velocity would produce sufficient material to account for the asymmetry. Depending upon how well-packed the regoliths of the parent bodies in the ring are, the regoliths would need to be centimeters- to meters-thick in order to hold all of this material.

At this time it is not clear whether collisions between parent bodies or collisions between parent bodies and external impactors are capable of providing enough extra ring material to produce the azimuthal asymmetry seen in the Galileo data. The two principal difficulties in deciding between these two models is our poor knowledge of the size distribution of the macroscopic particles in the main ring and the weak constraints on the impactor flux of the appropriate size range at Jupiter. Clearly, the assumption that the size distribution of the parent bodies is mono-modal is a poor one. The main ring's 1×10^{-6} optical depth will not all be contained in 10-m bodies. A more realistic size distribution will have far fewer small particles than large ones. Thus, for a given impactor flux, our collision frequencies are all upper limits. What is needed is a determination of the number of parent bodies of sufficient size to produce the asymmetry. Unfortunately, the upper limit on the number of macroscopic ring particles derived by Tyler et al. (1981) from Voyager radio observations is not stringent enough to allow us to decide between these two models.

6. Discussion

Comparison of the analyses of Voyager and Galileo data reveals a coherent picture of Jupiter's main ring. It is a tenuous ring with a normal optical depth, $\tau \sim$ a few $\times 10^{-6}$. It is also clear that the size distribution of the main ring particles is more complex than suggested by analysis of the Voyager data. Our photometric fits to the NIMS data and those of McMuldroch et al. (2000) show that the particle size distribution of the dusty grains in Jupiter's main ring cannot be completely described with a single power law. Our analysis of the NIMS data indicates that the ring particle size distribution is better described by a power law with a relatively shallow index that switches over to a steeper one beyond some particle size, than by a single power law distribution. The distributions we derive typically have a power law index between 2.0 and 3.0 in the tenths of a micron- and micron-size range and switch over to a significantly steeper one for particles tens of microns in size and larger.

At first glance, it might seem that our results are at odds with those of McMuldroch et al. (2000). They conclude that the NIMS data are best fit by a size distribution which is the

Table 5
Interparticle collision timescales in the main ring

Parent body size (m)	n_{pb}	t_{coll} (days)	v_{coll} (year^{-1})
10	2×10^7	0.002	10^5
100	2×10^5	0.2	10^3
1000	2×10^3	20	10^1

combination of two separate components. The first is a steep power law distribution with $q = 3.9 \pm 0.2$; the second is a log-normal distribution of particles between 0.6 and 18.0 μm with a mean particle size of 4.5 ± 0.2 μm and a standard deviation of 2.4 ± 0.4 μm. However, Fig. 13 shows that there are similarities between our derived distribution and that of McMuldroch et al. (2000). It is only below $\lesssim 1.0$ μm where our distribution and that of McMuldroch et al. (2000) begin to differ significantly. Above this size, the most significant difference between the distribution that we derived from the NIMS spectra and that of McMuldroch et al. (2000) is in the way in which they have been described. For both distributions, the slopes between ~ 1 and ~ 15 μm are relatively shallow; above this the distributions roll over and their slopes become much more steep. However, our distribution is also consistent with that of Showalter et al. (1987) at particle sizes less than 15 μm. At the phase angles and wavelengths of the Voyager observations, the sub-micron- and micron-sized particles dominate the scattering behavior. Thus, this is the portion of the distribution best constrained by the Voyager results. The distribution we derived from the NIMS data is also consistent with the results of our photometric analysis of the Galileo SSI data.

Ultimately, the size distribution of the ring particles is dictated by the production and loss processes that shape the ring. The observed distribution is proportional to the product of the particle lifetimes, $T(r)$, and production rates, $\dot{n}(r)$ (Horányi and Cravens, 1996),

$$n(r)\,dr \propto T(r)\dot{n}(r)\,dr. \tag{16}$$

Size-dependent loss processes have been identified that can affect the observed size distribution. In the models of Burns et al. (1999) and Horányi and Cravens (1996), ring particles drift inward towards Jupiter and are eventually lost to the planet's atmosphere. Poynting–Robertson drag is the dominant interaction in the Burns et al. model. As ring particles drift inward, Lorentz resonances, particularly the vertical 3 : 2 Lorentz resonance located at 122,150 km, are thought to pump up the inclinations of micron-sized particles, creating the structure of the main ring/halo transition region (Burns et al., 1985; Schaffer and Burns, 1987; Hamilton, 1994). The decay timescales for ring particle orbits evolving under Poynting–Robertson drag are proportional to particle size, r (Mignard, 1984).

Horányi and Cravens (1996) followed the orbits of ring particles between 0.1 and 10 μm in radius in a dynamical simulation that combined the effects of planetary oblateness, radiation pressure and magnetospheric perturbations. In their model, particles gain charge through the emission of photoelectrons stimulated by solar ultraviolet radiation. The particles' eccentric orbits cause the particles to sample regions of the magnetosphere with differing plasma parameters. As they sample these regions, they find themselves out of charge equilibrium with their surroundings and, because of their finite capacitance, they are unable to come into

charge balance before their orbits are perturbed. These perturbations cause them to sample broader regions in which they are further out of equilibrium and even more strongly perturbed by the planet's magnetic field. As a result, Horányi and Cravens find that jovian ring particles quickly lose energy and angular momentum and, as their semimajor axes decrease and their eccentricities increase, they are lost to Jupiter's atmosphere. As they spiral inward, their inclinations increase significantly as well (Horányi and Cravens, 1996, Fig. 2). In this model, orbital decay timescales are approximately $100\,(r/1\,\mu\text{m})^3$ days.

Canup et al. (1993) modeled the effects of radiation pressure and planetary oblateness on a distribution of ring particles released from a large parent body. Whereas the larger particles do not move far from the parent body, small particles rapidly (~ 12 years) develop significant eccentricities that increase their motion relative to the parent body. This evolution of the particles' eccentricities subsequently leads to a size-dependent rate of re-collision with the parent body for particles within a given size range. For a distribution of particles in the vicinity of Jupiter's main ring and a parent body the size of Adrastea, they found that this size-dependent collision rate went as r for particles between 11 and ~ 1000 μm in radius and leads to a steepening of the size distribution in this range.

If ring particles are continuously produced, the processes described above would alter the initial size distribution of the ring particles in fairly straightforward ways. At particle sizes for which orbital decay rates exceed production rates, production will determine the size distribution of the observed ring particles (i.e., particles cannot be lost faster than they are produced). For sizes such that production rates exceed loss rates, however, the size distribution will reflect a balance between production and loss, as described by Eq. (16). Thus, the Burns et al. model would predict a decrease in the slope of the size distribution by 1 at those sizes. That of Horányi and Cravens would predict a size distribution with a slope shallower by 3 than it would otherwise be. The Canup et al. model predicts a steepening of the size distribution by 1 for particles larger than 11 μm, a value roughly consistent with the value we have determined for r_{brk}. Thus, it seems possible that one or more of the processes described in these models could produce the size distribution we have derived from the Galileo SSI and NIMS observations.

If, however, the ring was created by the catastrophic break up of a large progenitor body sometime in the past and there has been little or no replenishment of the smallest ring grains since, production rates cannot be viewed as having been constant over the lifetime of the ring. In this case, one might expect r_{brk} to evolve to larger grain sizes as more of the large particles are lost. In this scenario, the location of the break in the distribution would give an approximate age for the ring. According to the model of Horányi and Cravens, in which particles of 1 μm are lost in just 100 days, the main ring would be young, ~ 1000 years. The ring would still be

relatively young, $\sim 10^6$ years, if the rates from Burns et al. (1999) apply.

The actual situation is more complex than this. Values suggested for the power law index appropriate to the production of collisional ejecta vary widely. And, debate persists as to whether the model of Burns et al. (1999) or that of Horányi and Cravens (1996) more closely describes the evolution of Jupiter's main ring. These two mechanisms operate on very different timescales. Sputtering, which is thought to operate on timescales between 100 and 10,000 years for 1-μm particles (Burns et al., 1999), is unlikely to play a significant role for particles smaller than 10 μm in the Horányi and Cravens model. On the other hand, at Jupiter's distance from the Sun, Poynting–Robertson drag causes micron-sized particles to spiral inward at a more leisurely 10^5 year timescale (Jewitt and Danielson, 1981; Burns et al., 1984). Therefore, in the Burns et al. model, where Poynting–Robertson drag dominates, sputtering should probably be taken into account. However, the large uncertainties in the physical properties of the magnetosphere so close to Jupiter make this difficult to do. The Canup et al. model assumed that the parent body was on a circular orbit and does not take into account the eccentricity of Adrastea. Nor did it include the presence of Metis. Any parent bodies in the main ring will act as additional sources and sinks for ring particles. Additionally, Metis, Adrastea and large parent bodies may stir up the ring particles to sufficiently high eccentricities that the effects observed by Canup et al. (1993) may not occur.

We have confirmed the existence of the near arm/far arm asymmetry reported by Ockert-Bell et al. (1999). However, there are differences between the asymmetry seen in the Galileo SSI data and that reported by Showalter et al. (1987). In the Galileo images, it is the near arm of the ring that appears brighter than the far one; the opposite is the case in the Voyager images. Whereas the asymmetry increases towards the ansa in the Voyager images, the asymmetry is strongest furthest from the ansa in the Galileo images. This and the fact that the asymmetry is not apparent in all of the data suggest that the asymmetry is more of a regional, azimuthal asymmetry rather than one related to the ring arms. This broad azimuthal asymmetry and the smaller "patches" reported on by Ockert-Bell et al. (1999) represent intriguing phenomena that have yet to be explained.

7. Conclusions

We agree with the conclusion of McMuldroch et al. (2000) that the NIMS data suggest that the size distribution of the jovian main ring particles is more complex than a power law distribution over the 0.01 to 100 μm size range. However, whereas they choose to describe the size distribution as the superposition of a steep power law and a log-normal distribution, we prefer a model in which the size distribution is a shallow power law that transitions to a steeper one above some cutoff size. The size distribution of the particles in Jupiter's main ring is the result of the various production and loss processes that act on the ring. One straightforward interpretation of our derived size distribution is that it is the result of size-dependent loss processes acting on a collisionally-derived power law size distribution.

The jovian main ring possesses azimuthal asymmetries on at least two scales. Small scale asymmetries appear as bright patches in images of the ring's ansae. A larger scale asymmetry becomes apparent when one compares the radially-integrated brightness of the ring at different longitudes. Of the mechanisms we have examined to explain the broad scale asymmetries observed, the release of debris in collisions either between parent bodies in the main ring or between parent bodies and external impactors are most consistent with the observations. It may be that the smaller scale brightness patches are the debris generated by smaller, less energetic collisions.

Images taken of the main ring at low phase angles during orbits G28 and G29 of the Galileo Extended Mission show a markedly different profile than do the high phase angle images from C3 (Brooks, 2003; Burns et al., 2004). That observing geometry emphasizes the macroscopic portion of the distribution and may represent the parent bodies that produce the micron-sized dust seen in forward-scatter. If this is the case, the differences in the radial profiles may reflect the action of some transport process or processes. We intend to model dust transport processes in the ring system and reproduce the basic features that have been observed. Using the radial profiles of the microscopic and macroscopic ring particles, as well as the size distribution of the micron-sized ring grains, as constraints, we hope to further our understanding of which processes shape the jovian ring system.

Acknowledgments

References

Acuña, M.H., Ness, N.F., 1976. The complex main magnetic field of Jupiter. J. Geophys. Res. 81, 2917–2922.

Barbara, J.M., Esposito, L.W., 2002. Moonlet collisions and the effects of tidally modified accretion in Saturn's F ring. Icarus 160, 161–171.

Belton, M.J.S., Klaasen, K.P., Clary, M.C., Anderson, J.L., Anger, C.D., Carr, M.H., Chapman, C.R., Davies, M.E., Greeley, R., Anderson, D., Bolef, L.K., Townsend, T.E., Greenberg, R., Head III, J.W., Neukum, G., Pilcher, C.B., Veverka, J., Gierasch, P.J., Fanale, F.P., Ingersoll, A.P., Masursky, H., Morrison, D., Pollack, J.B., 1992. The Galileo solid-state imaging experiment. Space Sci. Rev. 60, 413–455.

Bierhaus, E.B., Chapman, C.R., Merline, W.J., Brooks, S.M., Asphaug, E., 2001. Pwyll secondaries and other small craters on Europa. Icarus 153, 264–276.

Bohren, C.F., Huffman, D.R., 1983. Absorption and Scattering of Light by Small Particles. Wiley, New York.

Brooks, S.M., 2003. Jupiter's ring system revisited: a deeper understanding from Galileo visible and infrared observations. PhD thesis. University of Colorado, Boulder, CO.

Burns, J.A., Showalter, M.R., Morfill, G.E., 1984. The ethereal rings of Jupiter and Saturn. In: Greenberg, R., Brahic, A. (Eds.), Planetary Rings. Univ. of Arizona Press, Tucson, pp. 200–272.

Burns, J.A., Schaffer, L.E., Greenberg, R.J., Showalter, M.R., 1985. Lorentz resonances and the structure of the jovian ring. Nature 316, 115–119.

Burns, J.A., Showalter, M.R., Hamilton, D.P., Nicholson, P.D., de Pater, I., Ockert-Bell, M.E., Thomas, P.C., 1999. The formation of Jupiter's faint rings. Science 281, 1146–1150.

Burns, J.A., Simonelli, D.P., Showalter, M.R., Hamilton, D.P., Esposito, L.W., Porco, C.C., 2004. Jupiter's ring–moon system. In: Bagenal, F., McKinnon, W., Dowling, T. (Eds.), Jupiter: Planets, Satellites & Magnetosphere. Cambridge Univ. Press, Cambridge. In press.

Canup, R.M., Colwell, J.E., Horányi, M., 1993. Size distributions of satellite dust ejecta: effects of radiation pressure and planetary oblateness. Icarus 105, 363–369.

Carlson, R.W., Weissman, P.R., Smythe, W.D., Mahoney, J.C., the NIMS Science and Engineering Teams, 1992. Near-infrared mapping spectrometer experiment on Galileo. Space Sci. Rev. 60, 457–502.

Carlson, R.W., Drossart, P., Encrenaz, Th., Weissman, P.R., Hui, J., Segura, M., 1997. Temperature, size and energy of the Shoemaker–Levy 9 G-impact fireball. Icarus 128, 251–274.

Chandrasekhar, S., 1960. Radiative Transfer. Dover, New York.

Cuzzi, J.N., Burns, J.A., 1988. Charged particle depletion surrounding Saturn's F ring: evidence for a moonlet belt? Icarus 74, 284–324.

Cuzzi, J.N., Estrada, 1998. Compositional evolution of Saturn's rings due to meteoroid bombardment. Icarus 132, 1–35.

Cuzzi, J.N., Lissauer, J.J., Esposito, L.W., Holberg, J.B., Marouf, E.A., Tyler, G.L., Boischot, A., 1984. Saturn's rings: properties and processes. In: Greenberg, R., Brahic, A. (Eds.), Planetary Rings. Univ. of Arizona Press, Tucson, pp. 73–199.

Danielson, G.E., Kupferman, P.N., Johnson, T.V., Soderblom, L.A., 1981. Radiometric performance of the Voyager cameras. J. Geophys. Res. 86, 8683–8689.

de Pater, I., Showalter, M.R., Burns, J.A., Nicholson, P.D., Liu, M.C., Hamilton, D.P., Graham, J.R., 1999. Keck infrared observations of Jupiter's ring system near Earth's 1997 ring plane crossing. Icarus 138, 214–223.

Fillius, R.W., McIlwain, C.E., Mogro-Campero, A., 1975. Radiation belts of Jupiter—a second look. Science 188, 465–467.

Greenberg, R., Wacker, J.F., Hartmann, W.K., Chapman, C.R., 1978. Planetesimals to planets: numerical simulation of collisional evolution. Icarus 35, 1–26.

Grün, E., Morfill, G., Schwehm, G., Johnson, T.V., 1980. A model of the origin of the jovian ring. Icarus 44, 326–338.

Hamilton, D.P., 1994. A comparison of Lorentz, planetary gravitational, and satellite gravitational resonances. Icarus 109, 221–240.

Hansen, J.E., Travis, L.D., 1974. Light scattering in planetary atmospheres. Space Sci. Rev. 16, 527–610.

Horányi, M., Cravens, T.E., 1996. The structure and dynamics of Jupiter's ring. Nature 381, 293–295.

Jewitt, D.C., Danielson, G.E., 1981. The jovian ring. J. Geophys. Res. 86, 8691–8697.

Klaasen, K.P., Clary, M.C., Janesick, J.R., 1984. Charge-coupled device television camera for NASA's Galileo mission to Jupiter. Opt. Eng. 23, 334–342.

Klaasen, K.P., Belton, M.J.S., Breneman, H.H., McEwen, A.S., Davies, M.E., Sullivan, R.J., Chapman, C.R., Neukum, G., Heffernan, C.M., Harch, A.P., Kaufman, J.M., Merline, W.J., Gaddis, L.R., Cunningham, W.F., Helfenstein, P., Colvin, T.R., 1997. Inflight performance characteristics, calibrations, and utilization of the Galileo SSI camera. Opt. Eng. 36, 3001–3027.

Klaasen, K.P., Breneman, H.H., Cunningham, W.F., Kaufman, J.M., Klemaszewski, J.E., Magee, K.P., McEwen, A.S., Mortensen, H.B., Pappalardo, R.T., Senske, D.A., Sullivan, R.J., Vasavada, A.R., 1999. Calibration and performance of the Galileo solid-state imaging system in Jupiter orbit. Opt. Eng. 38, 1178–1199.

Marouf, E.A., Tyler, G.L., Zebker, H.A., Simpson, R.A., Eschelman, V.R., 1983. Particle size distributions in Saturn's rings from Voyager 1 radio occultation. Icarus 54, 189–211.

McMuldroch, S., Pilorz, S.H., Danielson, G.E., 2000. Galileo NIMS near-infrared observations of Jupiter's ring system. Icarus 146, 1–11.

Menke, W., 1984. Geophysical Data Analysis: Discrete Inverse Theory. Academic Press, Orlando, FL.

Meier, R., Smith, B.A., Owen, T.C., Becklin, E.E., Terrile, R.J., 1999. Near infrared photometry of the jovian ring and Amalthea. Icarus 141, 253–262.

Mignard, F., 1984. Effects of radiation forces on dust particles in planetary rings. In: Greenberg, R., Brahic, A. (Eds.), Planetary Rings. Univ. of Arizona Press, Tucson, pp. 333–366.

Neugebauer, G., Becklin, E.E., Jewitt, D., Terrile, R., Danielson, G.E., 1981. Spectra of the jovian ring and Amalthea. Astron. J. 86, 607–610.

Nicholson, P.D., Matthews, K., 1991. Near-infrared observations of the jovian ring and small satellites. Icarus 93, 331–346.

Ockert-Bell, M.E., Burns, J.A., Dunbar, I.J., Thomas, P.C., Veverka, J., Belton, M.J.S., Klaasen, K.P., 1999. The structure of Jupiter's ring system as revealed by the Galileo imaging experiment. Icarus 138, 188–213.

Pollack, J.B., Cuzzi, J.N., 1980. Scattering by nonspherical particles of size comparable to a wavelength: a new semi-empirical theory and its application to tropospheric aerosols. J. Atmos. Sci. 37, 868–881.

Porco, C.C., West, R.A., McEwen, A.S., Del Genio, A.D., Ingersoll, A.P., Thomas, P., Squyres, S., Dones, L., Murray, C.D., Johnson, T.V., Burns, J.A., Brahic, A., Neukum, G., Veverka, J., Barbara, J.M., Denk, T., Evans, M., Ferrier, J.J., Geissler, P., Helfenstein, P., Roatsch, T., Throop, H.B., Tiscareno, M., Vasavada, A.R., 2002. Cassini imaging of Jupiter's atmosphere, satellites and rings. Science 299, 1541–1547.

Schaffer, L., Burns, J.A., 1987. The dynamics of weakly charged dust: motion through Jupiter's gravitational and magnetic fields. J. Geophys. Res. 92, 2264–2280.

Showalter, M.R., 1985. Jupiter's ring system resolved: physical properties inferred from the Voyager images. PhD thesis. Cornell University, Ithaca, NY.

Showalter, M.R., 1998. Detection of centimeter-sized meteoroid impact events in Saturn's F ring. Science 282, 1099–1102.

Showalter, M.R., Burns, J.A., Cuzzi, J.N., Pollack, J.B., 1985. Discovery of Jupiter's gossamer ring. Nature 316, 526–528.

Showalter, M.R., Burns, J.A., Cuzzi, J.N., Pollack, J.B., 1987. Jupiter's ring system: new results on structure and particle properties. Icarus 69, 458–498.

Thompson, W.T., Lumme, K., Irvine, W.M., Esposito, L.W., 1981. Saturn's rings: azimuthal variations, phase curves and radial profiles in four colors. Icarus 46, 187–200.

Throop, H.B., Porco, C.C., 2001. Cassini observations of Jupiter's rings. Bull. Am. Astron. Soc. 33, 1095–1096. Abstract.

Tyler, G.L., Marouf, E.A., Wood, G.E., 1981. Radio occultation of Jupiter's ring—bounds on optical depth and particle size and a comparison with infrared and optical results. J. Geophys. Res. 86, 8699–8703.

van de Hulst, H.C., 1957. Light Scattering by Small Particles. Dover, New York, NY. Reprinted 1981.

Zahnle, K., Schenk, P., Levison, H.F., Dones, L., 2003. Cratering rates in the outer Solar System. Icarus 163, 263–289.

Further reading

Bosh, A.S., Rivkin, A.S., 1996. Observations of Saturn's inner satellites during the May 1995 ring-plane crossing. Science 272, 518–521.

Nicholson, P.D., Showalter, M.R., Dones, L., French, R.G., Larson, S.M., Lissauer, J.J., McGhee, C.A., Seitzer, P., Sicardy, B., Danielson, G.E., 1996. Observations of Saturn's ring-plane crossings in August and November 1995. Science 272, 509–515.

Poulet, F., Sicardy, B., Nicholson, P.D., Karkoschka, E., Caldwell, J., 2000. Saturn's ring-plane crossings of August and November 1995: a model for the new F-ring objects. Icarus 144, 135–148.